Received: 18 June 2020 | Revised: 3 February 2021 | Accepted: 11 February 2021 | Published on: 4 March 2021

DOI: 10.1002/qj.4002

Quarterly Journal of the Royal Meteorological Society RMetS

RESEARCH ARTICLE

Arctic ocean–sea ice reanalysis for the period 2007–2016 using the adjoint method

Guokun Lyu[1,2] | **Armin Koehl**[1] | **Nuno Serra**[1] | **Detlef Stammer**[1] | **Jiping Xie**[3]

[1]Center for Earth System Research and Sustainability (CEN), University of Hamburg, Hamburg, Germany

[2]School of Oceanography, Shanghai Jiao Tong University, Shanghai, China

[3]Nansen Environmental and Remote Sensing Center, Bergen, Norway

Correspondence
G. Lyu, School of Oceanography, Shanghai Jiao Tong University, Huashan road 1954, Shanghai 200000, China.
Email: guokun.lyu@uni-hamburg.de

Abstract

We present an Arctic ocean–sea ice reanalysis covering the period 2007–2016 based on the adjoint approach of the Estimating the Circulation and Climate of the Ocean (ECCO) consortium. The spatiotemporal variation of Arctic sea surface temperature (SST), sea ice concentration (SIC), and sea ice thickness (SIT) is substantially improved after the assimilation of ocean and sea ice observations. By assimilating additional World Ocean Atlas 2018 (WOA18) hydrographic data, the freshwater content of the Canadian Basin becomes closer to the observations and translates into changes of the ocean circulation and of transports through the Fram and Davis straits. This new reanalysis compares well with previous filter-based (TOPAZ4) and nudging-based (PIOMAS) reanalyses regarding SIC and SST. Benefiting from using the adjoint of the sea ice model, our reanalysis is superior to the ECCOv4r4 product considering sea ice parameters. However, the mean state and variability of the freshwater content and the transport properties of our reanalysis remain different from TOPAZ4 and ECCOv4r4, likely because of a lack of hydrographic observations.

KEYWORDS

adjoint method, data assimilation, ocean–sea ice reanalysis

1 | INTRODUCTION

The Arctic Ocean is a hotspot in the changing Earth system and is experiencing rapid warming of surface air temperature (AMAP, 2019), changes in the freshwater content of the Canadian Basin (Proshutinsky *et al.*, 2019), changes in the mass exchange with the Atlantic Ocean (Dmitrenko *et al.*, 2008) and the Pacific Ocean (Woodgate *et al.*, 2012), and a dramatic decline in sea ice cover (Kwok, 2018). The sea ice coverage at the ocean–atmosphere interface modulates the heat, freshwater, and momentum fluxes and is potentially changing the heat and freshwater budgets of the Arctic system. Improving our understanding of the Arctic Ocean circulation and its changes, its interactions with sea ice and the atmosphere, and its exchanges with the Pacific and Atlantic oceans is crucial for making predictions and projections of Arctic changes.

Because of the harsh environmental conditions and diplomatic constraints, the Arctic Ocean remains one of the most undersampled regions of the global oceans. Although sea ice concentration (SIC) is observed by satellites every day, the sea ice cover limits hydrographic observations and degrades altimetry-based sea level observations (Armitage *et al.*, 2016; Rose *et al.*, 2019). The sparseness of observations limits their interpretation in terms of mechanisms and feedbacks in the Arctic Ocean.

Numerical model simulations, which provide spatiotemporally varying ocean states, are therefore used to complement in-situ and satellite observations and understand the Arctic Ocean variability and its causes. However, model simulations also suffer from model deficiencies, such as biases in transports (Fieg *et al.*, 2010; Aksenov *et al.*, 2016) and misrepresentations of the ice edge.

To further improve state-of-the-art numerical simulations of the Arctic Ocean circulation and, at the same time, to improve our interpretation of the sparse observations, models are being constrained by ocean observations through data assimilation techniques. Resulting ocean–sea ice reanalyses (e.g., Fenty and Heimbach, 2013; Fenty *et al.*, 2017; Koldunov *et al.*, 2017) provide an invaluable basis for assessing variability and trends of the Arctic sea ice cover (Chevallier *et al.*, 2017), and oceanic transports and their variability (Uotila *et al.*, 2019). However, analyzing the dynamics of the sea ice changes and the full freshwater budget of the Arctic remains difficult from the Arctic Ocean reanalyses.

A crucial factor in this context is that most of the coupled ocean–sea ice reanalyses are produced using sequential methods (so-called filters), which correct model state at the analysis steps and introduce mass and energy increments at each analysis step (see Stammer *et al.*, 2016 for a review on the methods). For instance, the Tracers of Phytoplankton with Allometric Zooplankton 4 (TOPAZ4) reanalysis (Sakov *et al.*, 2012; Xie *et al.*, 2017; Xie *et al.*, 2018) uses an ensemble Kalman filter to assimilate near-real-time observations, resulting in potential discontinuities in the time evolution of the model trajectory. In contrast, the Pan-Arctic Ice Ocean Modeling and Assimilation System (PIOMAS) reanalysis (Lindsay and Zhang, 2006) uses a nudging scheme to assimilate SIC observations and sea surface temperature (SST), thereby continuously adding source terms to the governing equations. Discontinuities introduced by the data assimilation are thereby alleviated. We cannot expect to obtain detailed dynamical insights into mechanisms leading to observed ocean–sea ice changes from both reanalyses.

In contrast, the adjoint method preserves model dynamics by bringing the model simulation close to observations through changing control variables. The resulting reanalysis is dynamically consistent over a long assimilation window (years to decades) (Stammer *et al.*, 2016). Applications of the adjoint method, excluding the assimilation of sea ice data, have been a mature field (Forget *et al.*, 2015; Köhl, 2015). Still, the incorporation of sea ice data remains challenging.

Great efforts have been made to implement the adjoint method to the coupled ocean–sea ice model (e.g., Heimbach *et al.*, 2010; Fenty and Heimbach, 2013), with encouraging results. However, the adjoint model may still suffer from strong sensitivities, which degrades the usefulness of the adjoint sensitivity, limits the number of iterations performed, and stalls the optimization process. For instance, Koldunov *et al.* (2017) reported that only five iterations could be performed in their Arctic ocean–sea ice assimilation system within a 1-year assimilation window because large sensitivities arose locally, rendering the adjoint sensitivity useless for the optimization algorithms. Because of this persisting problem, ECCO version 4 release 4 (ECCOv4r4, ECCO Consortium *et al.*, 2020a; 2020b, Forget *et al.*, 2015) excludes the adjoint of the sea ice model. Causes of the problem still need to be understood in detail, but they likely arise from linearizing nonlinear processes in the sea ice model.

Here, we use the adjoint method to constrain a coupled ocean–sea ice model by available observations. Building on the work of Koldunov *et al.* (2017), we aim to improve the previous setup of the Arctic reanalysis by modifying the adjoint model to enable more iterations over longer assimilation windows covering the period 2007–2016. In this work, we will examine the changes imposed in the model through the assimilation procedure and compare the resulting reanalysis against that of TOPAZ4 (Xie *et al.*, 2017) and PIOMAS (Lindsay and Zhang, 2006). Besides, we compare our reanalysis against that of ECCOv4r4 to illustrate the impact of using the adjoint of the sea ice model.

The data assimilation system and observations are described in section 2, together with the TOPAZ4, PIOMAS, and ECCOv4r4 reanalyses. In section 3, we assess the details of the model–data misfit reduction. Improvements in SIC and sea ice thickness (SIT) are evaluated and compared against the other three Arctic reanalyses in section 4. Section 5 focuses on ocean state changes concerning temperature, salinity, SST, freshwater content (FWC), and transports through the Fram Strait, Davis Strait, and the Barents Sea Opening. Comparisons with TOPAZ4 and ECCOv4r4 are also shown in this section. Adjustments of the control variables are examined in section 6. Section 7 provides concluding remarks.

2 | THE DATA ASSIMILATION SYSTEM AND OBSERVATIONS

This study builds on the coupled ocean–sea ice data assimilation system presented in the study of Koldunov *et al.* (2017). The system uses a pan-Arctic configuration of the Massachusetts Institute of Technology general circulation model (MITgcm) (Marshall *et al.*, 1997) coupled with a dynamic–thermodynamic sea ice model (see Losch *et al.*, 2010). The adjoint model is generated by the

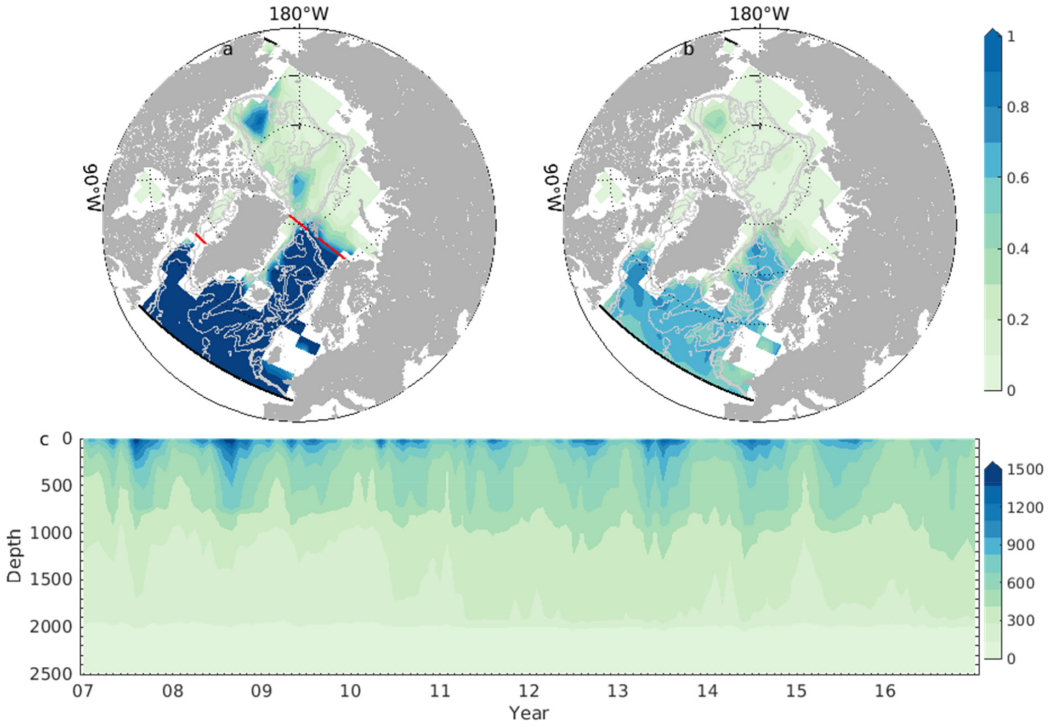

FIGURE 1 Model domain and profiles observing frequency (number/month) on a 3° × 3° grid from (a) April to October and (b) November to March. At most, one profile is counted each day on each grid. Panel (c) is the number of observations assimilated depending on time (per month) and depth. Red lines in panel (a) denote locations of Davis Strait, the Fram Strait, and the Barents Sea opening, where we compute volume, freshwater, and sea ice volume transports in section 5.3 [Colour figure can be viewed at wileyonlinelibrary.com]

Transformation of Algorithms in Fortran (TAF, Giering and Kaminski, 1998). It is then modified to stabilize the adjoint sensitivity when calculated over a 4-year assimilation window.

2.1 | The coupled ocean–sea ice model

The model domain covers the entire Arctic Ocean north of the Bering Strait and the Atlantic Ocean north of 44 °N (see Figure 1). The open boundaries are nested laterally into a 16-km Atlantic-Arctic configuration (Serra *et al.*, 2010). The system has 50 vertical z-levels ranging from 10 m at the surface to 456 m in the deep ocean. In the horizontal, a curvilinear grid with a resolution of ~16 km is used.

Atmospheric states from the 6-hourly National Centers for Environmental Prediction reanalysis 1 (NCEP-RA1) (Kalnay *et al.*, 1996), including 2-m air temperature, 10-m wind vectors, precipitation rate, 2-m specific humidity, downward longwave radiation, and net shortwave radiation, as well as bulk formulae, are used to compute the surface momentum, heat, and freshwater fluxes. The river runoff is applied near the river mouth with seasonally varying river discharge. A virtual salt flux parameterization is used to simulate the effects of freshwater input on salinity changes. The K-Profile scheme of Large *et al.* (1994) is used to parameterize unresolved vertical mixing effects.

The thermodynamic sea ice model is based on the zero-layer formulation of Semtner (1976) and Hibler (1980). The dynamic sea ice model is based on Hibler (1979) and is implemented following Zhang and Hibler (1997). The thermodynamic–dynamic sea ice model is then modified to apply adjoint data assimilation (Losch *et al.*, 2010; Fenty and Heimbach, 2013).

2.2 | The adjoint method

The adjoint model is used to bring the model simulation into consistency with available observations. The method minimizes a quadratic model–data misfit (also called cost function; Equation 1), weighted by the prior data uncertainties, by adjusting control variables iteratively.

$$\begin{aligned} J(C_{ini}, C_{atm}(t)) = & \sum_{t=1}^{T1} [y(t) - E(t)x(t)]^T R^{-1} [y(t) - E(t)x(t)] \\ & + C_{ini}^T P^{-1}(0) C_{ini} + \overline{C_{atm}}^T Q_m^{-1} \overline{C_{atm}} \\ & + \sum_{t=0}^{T1} C'_{atm}(t)^T Q_a^{-1} C'_{atm}(t) \end{aligned} \quad (1)$$

Over the whole reanalysis period (2007–2016), we adjust the initial condition of the year 2007 ($\mathbf{C_{ini}}$) and daily atmospheric states on the model grid ($\mathbf{C_{atm}(t)}$), which include 2-m air temperature, 2-m specific humidity, precipitation rate, 10-m wind vectors, downward longwave radiation, and net shortwave radiation.

On the right-hand side of Equation (1), the first term computes the uncertainty-weighted model–data misfits, where $\boldsymbol{y(t)}$ and $\boldsymbol{x(t)}$ represent observations and model state at time t, $\boldsymbol{E(t)}$ maps model states to the corresponding observations, and $\boldsymbol{R^{-1}}$ is an inverse error covariance matrix for observations. Superscript T denotes the transpose of the matrix. The remaining three terms penalize the adjustments of the initial state $\boldsymbol{C_{ini}}$, time-mean atmospheric forcing $\overline{\boldsymbol{C_{atm}}}$, and time-varying atmospheric forcing $\boldsymbol{C'_{atm}(t)}$ and are weighted by the square of prior uncertainties $\boldsymbol{P(0)}$, $\boldsymbol{Q_m}$, and $\boldsymbol{Q_a}$, respectively. Square of prior uncertainties of the initial state $\boldsymbol{P(0)}$ and the time-varying atmospheric forcing $\boldsymbol{Q_a}$ are computed as the variance of the nonseasonal variability of the corresponding variables using the WOA18 ocean atlas and the NCEP-RA1. Uncertainties of the mean component of 2-m air temperature, 2-m specific humidity, precipitation rate, 10-m wind vectors, downward longwave radiation, and net shortwave radiation are set to 1 °C, 0.001 kg·kg^{-1}, 1.5×10^{-8} mm·s^{-1}, 2 m·s^{-1}, 20 W·m^{-2}, and 20 W·m^{-2}.

Because of the computational limit and potential instability of the adjoint model, we separate the whole 10-year period (2007–2016) into three segments (2007–2010, 2010–2013, 2013–2016) with a 1-year overlap. A total number of $\sim10^9$ elements are adjusted in each chunk to reduce the cost function. The initial state of the latter segment is taken from the last iteration of the former segment to avoid discontinuities in the time evolution of the model trajectory when moving to the next segment.

To stabilize the adjoint model for a 4-year assimilation window, we made the following modifications to the adjoint of MITgcm:

1. Disable the K-profiles mixing parameterization scheme,
2. Use a free-drift sea ice dynamic model,
3. Increase the Laplacian diffusivity of heat and salinity to 500 m^2·s^{-1}, and lateral eddy viscosity to 10,000 m^2·s^{-1},
4. Apply a filter (Stammer *et al.*, 2018) to sensitivity variables calculated in the adjoint of the thermodynamic sea ice submodel (see details in Appendix).

A quasi-Newton algorithm based on Gilbert and Lemaréchal (2006) is used to iteratively reduce the cost function by adjusting the control variables employing the adjoint sensitivities. The optimization stops when the gradient descent algorithm cannot further reduce the cost function. The analyses discussed below are based on the zeroth iteration (referred to as "INTAROS-ctrl") and the last iteration (referred to as "INTAROS-opt") of the optimization.

2.3 | Observations and prior uncertainties

Both in situ and remote sensing observations are used to constrain the model simulation. Data sets that are assimilated and their sources are listed in Table 1.

The assimilated sea ice observations rely on satellite observations. SIC observations are derived from Advanced Microwave Scanning Radiometer for Earth Observing System (AMSR-E, 2007–2010), Special Sensor Microwave Imager (SSMI, 2011–2012), and Advanced Microwave Scanning Radiometer 2 (AMSR2, 2013–2016) (Kaleschke *et al.*, 2001; Spreen *et al.*, 2008). SIC uncertainties result from representation errors and observational errors (Fenty and Heimbach, 2013). Representation errors are assumed to be 15% within 50 km from the coastline and 10% over open water. Incorporating instrumental errors, we modify the errors by multiplicative factors of 0.85, 1.20, 1.10, and 1.00 for the observed SIC ranges of 0.00, <0.15, 0.15–0.25, and >0.25, respectively. SIT observations and their uncertainties are from the optimal-interpolated CryoSat-2/Soil Moisture and Ocean Salinity (SMOS) SIT product (Ricker *et al.*, 2017), which takes advantage of the high accuracy of SMOS-observed thin ice (<1 m) and CryoSat2-observed thick ice.

SST is based on optimal interpolated microwave and infrared data from the Remote Sensing System (RSS-SST). SST data are not available over the sea ice-covered region, but we assume SST is at freezing temperature (−1.96 °C) where sea ice is observed but not simulated. Uncertainties of SST result from representation errors, estimated based on the method of Oke and Sakov (2008), and observational errors (see Table 1). Along-track sea level anomaly observations from satellite altimetry are available over ice-free regions, and their uncertainties are set following Köhl (2015). Mean dynamic topography (Rose *et al.*, 2019) is assimilated to correct biases in the mean ocean circulation using uncertainties of 1 cm. Mapped sea level anomaly data over ice-covered regions (Rose *et al.*, 2019) is used to constrain the time-varying circulation using half of its standard deviation as the uncertainties.

For hydrographic data, the model is constrained to hydrographic profiles from EN4 data (Good *et al.*, 2013) and Unified Database for Arctic and Subarctic Hydrography (UDASH) data (Behrendt *et al.*, 2018). Duplicated data from the two hydrographic profile datasets are removed. On average, the Atlantic sector of the pan-Arctic Ocean is

TABLE 1 Data sets assimilated

Date sets	Variables abbreviations	Source
Mean dynamic topography	MDT	Rose *et al.* (2019), https://ftp.space.dtu.dk/pub/DTU19/MDT/
Daily sea surface temperature	SST	Remote Sensing System, http://www.remss.com/measurements/sea-surface-temperature/
ASI ice concentration	SIC SIC-SST[a]	Kaleschke *et al.* (2001) and Spreen *et al.* (2008), AMSRE (2007–2010), SSMI (2011–2012), AMSR2 (2013–2016), http://icdc.cen.uni-hamburg.de/1/daten/cryosphere.html
EN4 hydrographic data and UDASH	EN4-T EN4-S	Good *et al.* (2013), https://www.metoffice.gov.uk/hadobs/en4/ Behrendt *et al.* (2018), https://www.awi.de/forschung/klimawissenschaften/physikalische-ozeanographie/projekte/udash.html
SMOS and CryoSat-2 merged sea ice thickness	SIT	(Ricker *et al.*, 2017), https://spaces.awi.de/pages/viewpage.action?pageId=291898639
Along-track sea level anomaly	SLA	Copernicus Marine Environment Monitoring Service, http://marine.copernicus.eu
Monthly sea level anomaly over sea ice cover	SSH-Mon	Rose *et al.* (2019), https://ftp.space.dtu.dk/pub/ARCTIC_SEALEVEL/DTU_TUM_V3_2019/
Moorings	EN4-T[b] EN4-S[b]	Beaufort Gyre Exploration Project, https://www.whoi.edu/beaufortgyre Nansen and Amundsen Basin observational system, https://uaf-iarc.org/nabos/
WOA18	WOA-T WOA-S	Zweng *et al.* (2018), https://www.nodc.noaa.gov/OC5/woa18/woa18data.html

[a]Since SST is not observed in sea ice-covered regions, we assume SST is −1.96°C where sea ice is observed but not simulated in the model.
[b]Cost constituents of moorings are added to EN4 components in our analysis.

observed more than once per month per 3° × 3° box during April–October (Figure 1a) and once per 2 months during November–March (Figure 1b). However, hydrographic observations in ice-covered regions are much fewer than those in open water (Figure 1a,b). In the vertical, the profiles cover mainly the top 800 m (Figure 1c) and more observations are available in the summer season than in the winter season. Uncertainties of temperature and salinity profiles are the same as in Köhl (2015).

Additionally, the model simulation is constrained to the WOA18 climatology. Since the temperature and salinity climatology are interpolated to the finer grid, thereby inventing dependent data points, and the inverse covariance matrix is assumed diagonal, we reduced the weight of the temperature and salinity climatology cost components by a factor of 10 and 50, respectively. Although the resulting factors should have been the same for temperature and salinity, the values were adjusted to yield similar contributions to the cost function. Because of the low number of hydrographic profiles, we increased the weighting of the hydrological profile component by a factor of 10 to increase their relative importance with limited iterations.

2.4 | The TOPAZ4, PIOMAS, and ECCOv4r4 reanalyses

Available variables from the TOPAZ4 (Xie *et al.*, 2017), PIOMAS (Lindsay and Zhang, 2006), and ECCOv4r4 (Forget *et al.*, 2015; ECCO Consortium *et al.*, 2020a; ECCO Consortium *et al.*, 2020b) reanalyses are compared with our reanalysis. Table 2 lists the details of the three reanalyses. PIOMAS assimilates the least observations and the coarsest resolution among the three reanalyses. The data assimilation method in TOPAZ4 and INTAROS-opt are computationally more expensive than PIOMAS, and more observations are assimilated. ECCOv4r4 is a global ocean–sea ice reanalysis and also uses the adjoint method as our study. However, a major difference of ECCOv4r4 to our study is that it excludes the adjoint of the sea ice

TABLE 2 Details of the TOPAZ4, PIOMAS, and ECCOv4r4 reanalysis systems

	TOPAZ4	PIOMAS	ECCOv4r4
Ocean–sea ice model	HYCOM ocean-EVP ice dynamic model and thermodynamic model	Pan-Arctic ice ocean modeling and assimilation system	MITgcm ocean-LSR ice dynamic model and thermodynamic model
Resolution	12–16 km, 28 z-isopycnal layers	40 km, 21 vertical layers	~40 km in the Arctic Ocean, 50 vertical layers
Atmosphere forcing	ECMWF/ERA-Interim	NCEP/NCAR RA1	ECMWF/ERAInterim
Variables assimilated	SLA, SST, SIC, ice drift, SIT, in situ T/S	SIC, SST	SLA, MDT, in situ T/S, SST, SSS, SIC, OBP, WOA09
Data assimilation method	Ensemble Kalman filter	Mixed nudging and OI	Adjoint method
Reanalysis period	1991–now	1979–now	1992–2017

model (Forget *et al.*, 2015; ECCO Consortium *et al.*, 2020a; 2020b).

3 | EVALUATION OF THE OPTIMIZATION

The optimization involved running the coupled ocean–sea ice model forward to evaluate the cost function over the time frame 2007–2016, split into three segments as described above. The adjoint model integration then provides gradients of the cost function with respect to control parameters, which were used in an iterative way to minimize the model–data misfit. In the end, a total number of 15, 21, and 20 iterations were performed in the three segments, respectively.

Figure 2 shows the resulting percentage decrease in the total cost function and the individual cost components. The cost function is dominated by the constituents of sea surface temperature (SST), SIC, temperature (EN4-T) and salinity (EN4-S) profiles, and climatological temperature (WOA-T) and salinity (WOA-S), which is mainly due to a large number of these type of observations (SST, SIC, WOA-T, and WOA-S) and significant model–data misfits (EN4-T and EN4-S). The total cost reduction is more than 30% in the three segments. SST, SIC, and climatological temperature (WOA-T) and salinity (WOA-S) are reduced by 40–60%. The cost constituents of temperature (EN4-T) and salinity (EN4-S) profiles account for ~20 and ~10% of the total cost and are reduced by 30% and 60% upon assimilation, respectively. For the other constituents, MDT and SIT errors are reduced by more than 50%, but SLA and SIC-SST are degraded. Compared with Koldunov *et al.* (2017), the present optimization achieves a larger cost function reduction for the total and individual components. Besides starting from a better first-guess solution, the increased cost function reduction, in particular, results from the larger number of iterations performed here.

Because they appear to elicit the greatest improvement during the optimization, we focus on the improvements of SIC, SIT, and SST in the following section. We compare resulting fields with those available from the three reanalyses. Besides, model–data differences of hydrographic profiles, oceanic transports, and freshwater content are compared against TOPAZ4 and ECCOv4r4.

4 | SEA ICE PARAMETERS

4.1 | Sea ice concentration

The time series of sea ice area (SIA) shown in Figure 3a reveals a significant variation during the year, with more disagreements between simulations in wintertime and fairly consistent results during the summer minima. In particular, except for ECCOv4r4, all model simulations match the observed summer record-low SIA in 2007, 2012, and 2016. During the winter season, INTAROS-opt follows the satellite observations well, while the TOPAZ4 reanalysis underestimates SIA during the first 4 years and follows INTAROS-opt after that. PIOMAS also matches the observations well, but it slightly overestimates SIA in the winter season. In contrast, INTAROS-ctrl simulates more SIA than is observed. The ECCOv4r4 reanalysis overestimates SIA in the winter season and underestimates SIA in the summer season.

To reveal the winter intermodel discrepancies in more detail, Figure 3b shows SIA from January to March in 2007. TOPAZ4 clearly shows a 7-day signal caused by correcting the model state at the analysis step, characteristic of every filter approach. The POIMAS reanalysis shows more SIA than all the other simulations. Discontinuities are not visible in the PIOMAS reanalysis because they used a mixed nudging and optimal interpolation method to alleviate discontinuities. Yet, the nudging term still adds artificial sources and sinks to the model simulation and violates

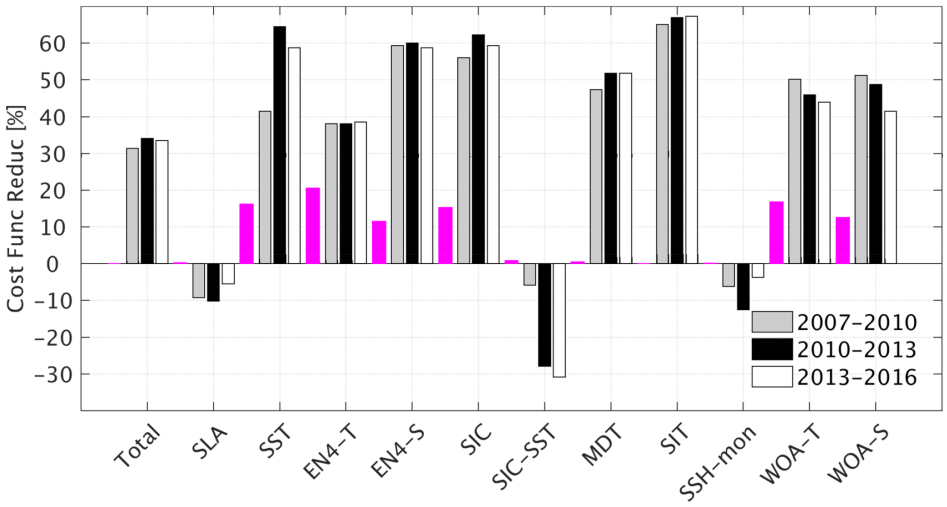

FIGURE 2 Percentage reduction of the total cost function and individual constituents in the three segments (see legend). The magenta bars denote contributions of the individual component to the entire cost function. Negative values indicate that the model–data misfits are increased for that type of observation [Colour figure can be viewed at wileyonlinelibrary.com]

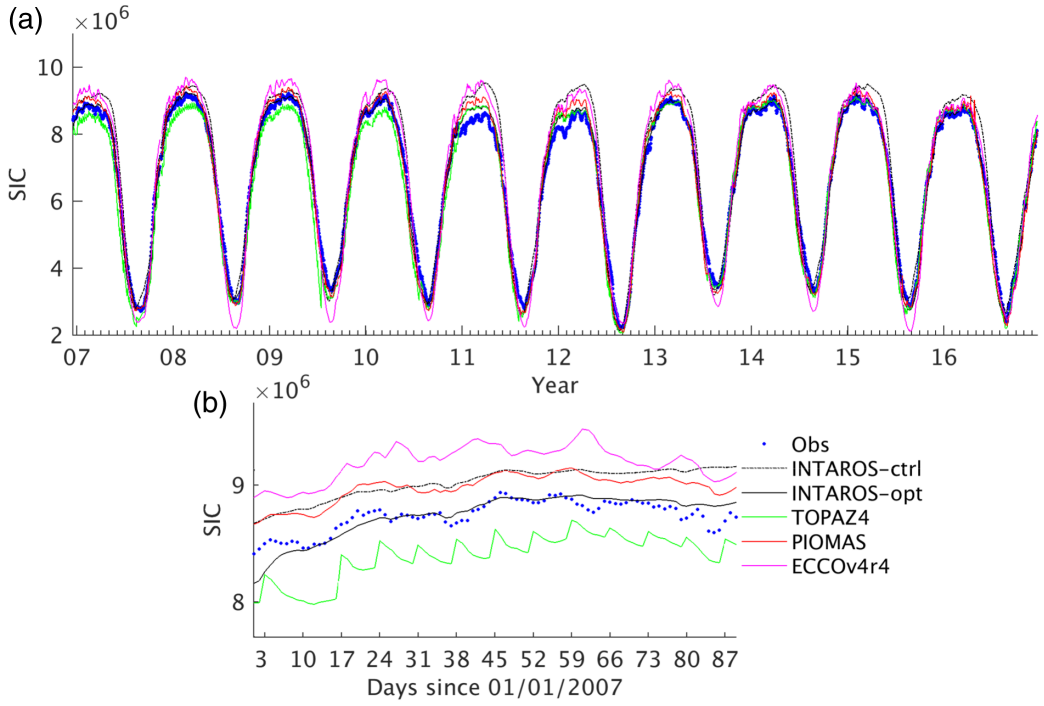

FIGURE 3 Total SIA over the model domain based on satellite observations (Obs), INTAROS-ctrl, INTAROS-opt, TOPAZ4, PIOMAS, and ECCOv4r4 (see legend). Panel (a) is for the whole reanalysis period (2007–2016), and panel (b) is for January–March, 2007 [Colour figure can be viewed at wileyonlinelibrary.com]

model physics. The ECCOv4r4 reanalysis simulates more SIA than all the other simulations. The INTAROS-opt brings the model-simulated SIA closest to the observations by adjusting the control variables.

Since SIA in the year 2012 reaches the record minimum, we take the year 2012 as an example to examine the spatial pattern of SIC in all the simulations. As expected, the spatial distribution of SIC is improved upon data assimilation (Figure 4a,e). In March, the sea ice edge extends more in INTAROS-ctrl (black dashed line in Figure 4a), a feature corrected through the assimilation process (shading in Figure 4a). Improvements in the spatial distribution of SIC are even more pronounced in September (Figure 4e). In contrast to the total SIA (Figure 3a), both TOPAZ4 (Figure 4b,f) and PIOMAS (Figure 4c,g) show an overall agreement with observations, considering the patterns and sea ice edge (15%). However, ECCOv4r4 (Figure 4d,h) matches the observation worse than all three ocean–sea ice reanalyses.

Overall, INTAROS-opt, TOPAZ4, and PIOMAS reproduce the total SIA minima in 2007, 2012, and 2016 and the spatial pattern of the pan-Arctic SIC. SIC in ECCOv4r4

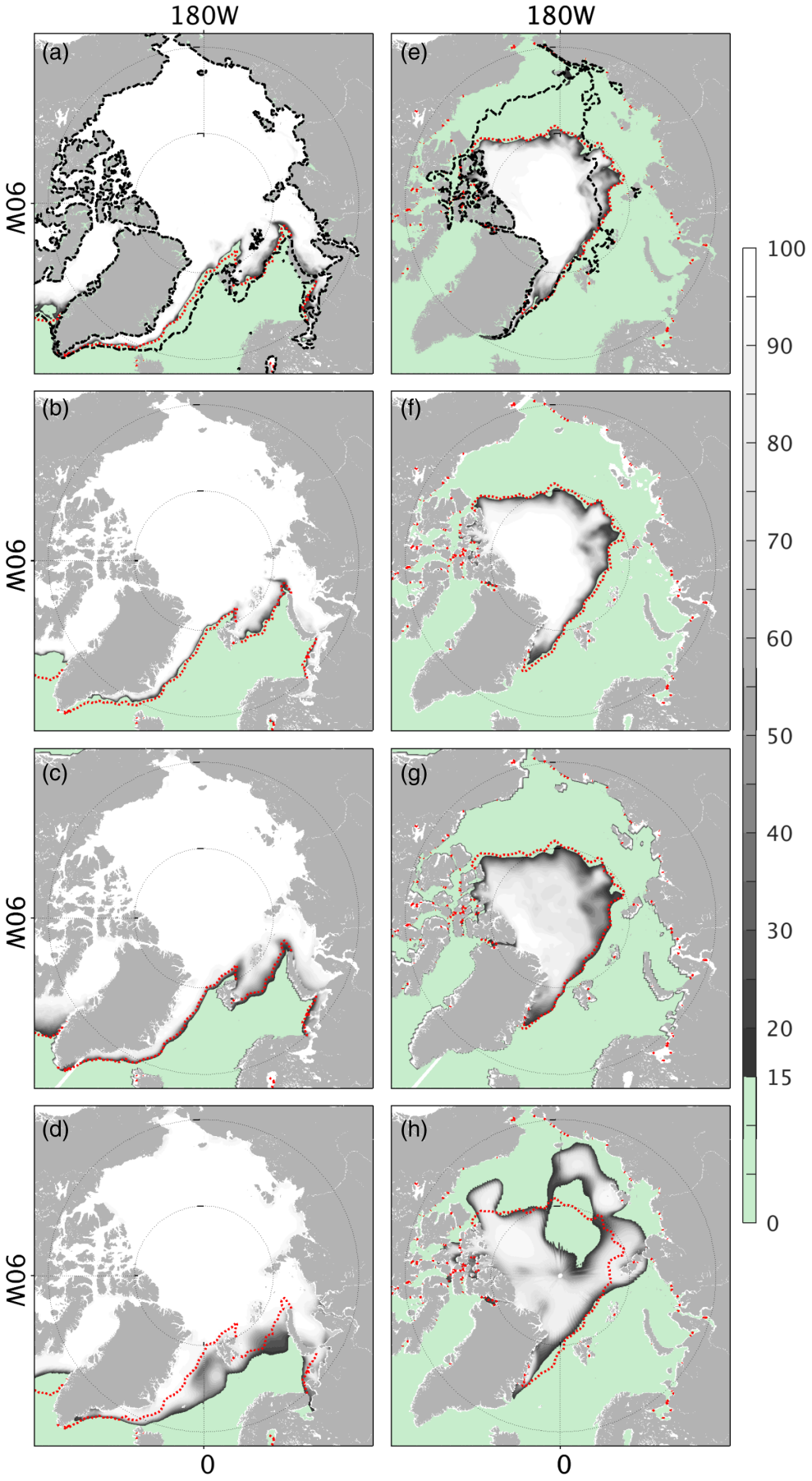

FIGURE 4 SIC in March, 2012 in (a) INTAROS-opt, (b) TOPAZ4, (c) PIOMAS, and (d) ECCOv4r4. Panels (e)–(h) are the corresponding September SIC. The red dotted lines are the satellite-observed sea ice edge (15%), and the black dashed lines in panels (a) and (e) are the sea ice edge in INTAROS-ctrl [Colour figure can be viewed at wileyonlinelibrary.com]

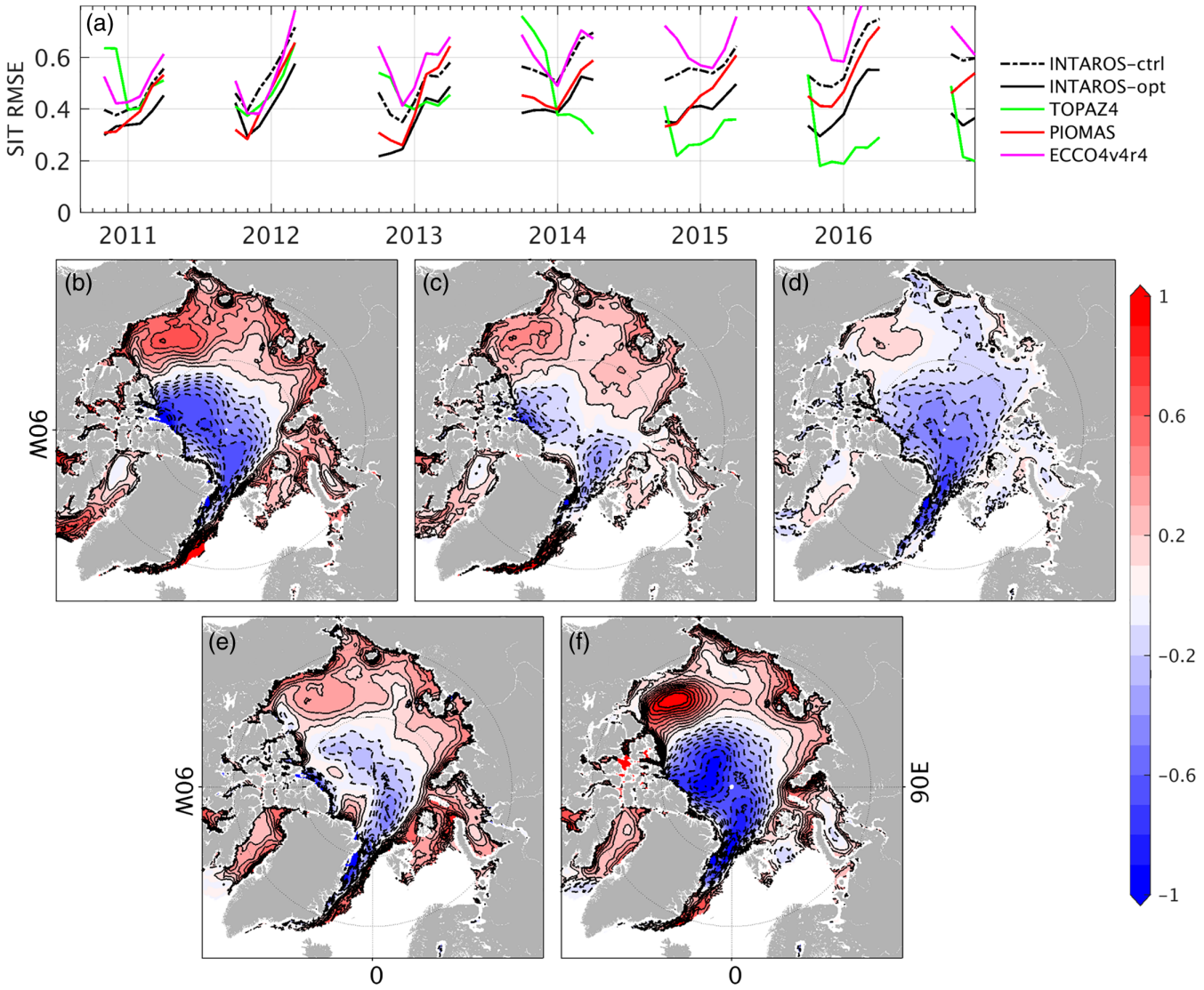

FIGURE 5 (a) RMSE between the CryoSat2-SMOS observations and INTAROS-ctrl, INTAROS-opt, TOPAZ4, PIOMAS, and ECCOv4r4. The remaining panels show the mean SIT differences between CryoSat2-SMOS merged data and (b) INTAROS-ctrl, (c) INTAROS-opt, (d) TOPAZ4, (e) PIOMAS, and (f) ECCOv4r4. The contour interval is 0.1 m [Colour figure can be viewed at wileyonlinelibrary.com]

is significantly different from satellite observation, which can be attributed to the exclusion of the adjoint of the sea ice model. The adjoint of the sea ice model was not incorporated in the ECCOv4r4 because of the associated difficulties, which the present article largely resolved.

4.2 | Sea ice thickness and volume

SIT differences remain large among different ocean–sea ice reanalyses (Chevallier *et al.*, 2017), which may be caused by differences in sea ice models and how SIT is updated when ingesting observations by data assimilation. In this section, we analyze improvements to SIT due to the adjustment of the control variables and compare them with TOPAZ4, PIOMAS, and ECCOv4r4.

The cost of SIT is reduced by ~60% in the three segments (Figure 2), despite its very small contribution to the total cost. INTAROS-ctrl (Figure 5b) underestimates mean SIT in the central Arctic Ocean and north of Greenland, covered by multiple-year sea ice, and overestimates mean SIT over seasonal sea ice extent regions. INTAROS-opt reduces mean SIT errors significantly (Figure 5c), and the root mean square error (RMSE) is reduced from 0.54 m in INTAROS-ctrl to 0.40 m in INTAROS-opt (Figure 5a).

PIOMAS shows a slightly larger RMSE of SIT (0.46 m) than INTAROS-opt (0.40 m) and TOPAZ4 (0.41 m, Figure 5a). TOPAZ4 shows larger errors in October and November than both INTAROS-opt and PIOMAS, but the SIT errors are quickly reduced as the model assimilates observations sequentially, resulting in smaller RMSE than both PIOMAS and INTAROS-opt at the start of

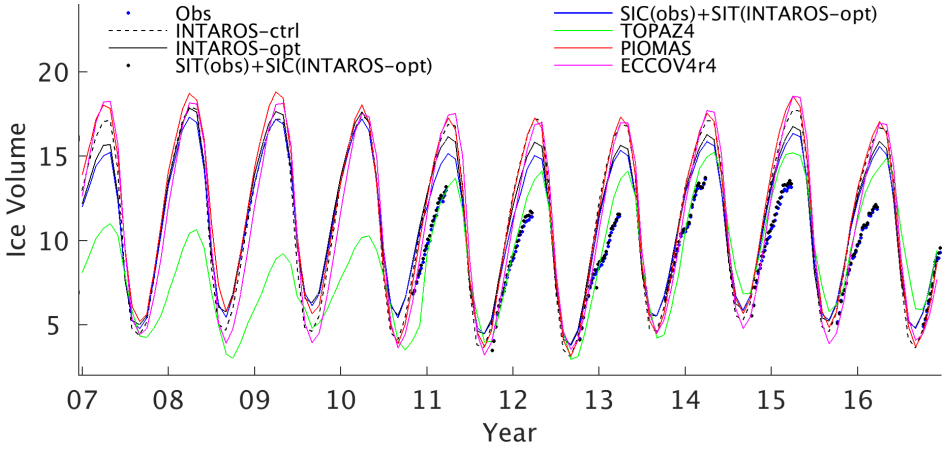

FIGURE 6 Total sea ice volume over the model domain based on CrySat2-SMOS merged product (Obs), INTAROS-ctrl, INTAROS-opt, TOPAZ4, PIOMAS, and ECCOv4r4 (see legend). Also presented are total sea ice volume using observed SIC and SIT in INTAROS-opt (blue line), observed SIT, and SIC in INTAROS-opt (black dotted line) [Colour figure can be viewed at wileyonlinelibrary.com]

the next year. Again, ECCOv4r4 shows the largest SIT errors (Figure 5a,f), which are even larger than those of INTAROS-ctrl.

Mean SIT bias remains in the three products. Negative SIT errors up to −0.6 m exist in the central Arctic Ocean and the Eurasian Basin, extending to the northeastern Greenland coast. In the Beaufort Sea, all four reanalyses overestimate SIT by ~0.2–1.0 m, with TOPAZ4 performing best. In the seasonal sea ice extent regions, including the marginal seas and around Greenland, TOPAZ4 data show smaller mean SIT errors than the other three reanalyses.

Despite the improvements in SIC and SIT, we note that sea ice volume shows significantly different time variability among different reanalyses (Figure 6). For instance, our model simulations, ECCOv4r4, and PIOMAS show a more substantial seasonal variation than does the TOPAZ4 data, especially before 2011. INTAROS-opt changes the total sea ice volume in the summer season throughout the 10 years and in the winter season after 2010 when additional SIT observations are available. Despite the different assimilation methods and numerical models, we see that the state-of-the-art ocean–sea ice models reproduce the spatiotemporally varying SIC successfully. We speculate that SIT is improved either through rectifying mechanisms by improvements on SIC or by assimilating additional SIT data in the winter season. The beneficial effects of assimilating satellite SIT are more clearly visible in the TOPAZ4 reanalysis after January of the year 2014.

To examine the relative importance of SIC and SIT on the residual sea ice volume, we replace each component in INTAROS-opt with observations (blue line and black dots in Figure 6). Replacing SIT with observations (black dots in Figure 6) achieves a better match with the observed sea ice volume than replacing SIC with observations (blue line in Figure 6), indicating that the sea ice volume improvement mostly results from the SIC assimilation and that SIT needs to be further improved to further reduce sea ice volume error.

5 | OCEAN STATE

In the filter approaches, ocean states are changed by updating the state through assimilating observations and propagating the analysis increment by the forward model. The adjoint method adjusts the atmospheric forcing and the initial state to reduce the model–data misfits. These adjustments to the control variables are calculated by the information propagated by the adjoint model and the forward model. This section concentrates on ocean changes after data assimilation and compares them with TOPAZ4 and ECCOv4r4.

5.1 | Model–data differences in temperature and salinity

Based on INTAROS-ctrl, INTAROS-opt, TOPAZ4, and ECCOv4r4, we compute RMSEs of temperature (Figure 7a) and salinity (Figure 7b) to the profile observations and averaged them over our model domain and the years 2007–2016. In INTAROS-opt, both temperature (Figure 7a) and salinity (Figure 7b) errors are reduced in the top 3,000 m upon data assimilation. Both TOPAZ4 and ECCOv4r4 show overall smaller RMSEs of temperature and salinity in the top 3,000 m than INTAROS-opt. For ocean temperature (Figure 7a), ECCOv4r4 shows larger temperature errors in the top 30 m and is comparable to the TOPAZ4 in the layer 50–250 m and has the smallest errors below. Salinity RMSEs (Figure 7b) reveal that ECCOv4r4 has smaller salinity errors except for the ocean surface, where TOPAZ4 shows even smaller salinity errors.

Temperature differences (Figure 8) of the four simulations relative to the profiles in the layer 100–1,000 m are examined. INTAROS-ctrl (Figure 8a) simulates a warmer intermediate layer, and the biases can be up to 2 °C in the Arctic Atlantic water and 1 °C in the Atlantic Ocean. INTAROS-opt (Figure 8b) significantly reduces warm bias,

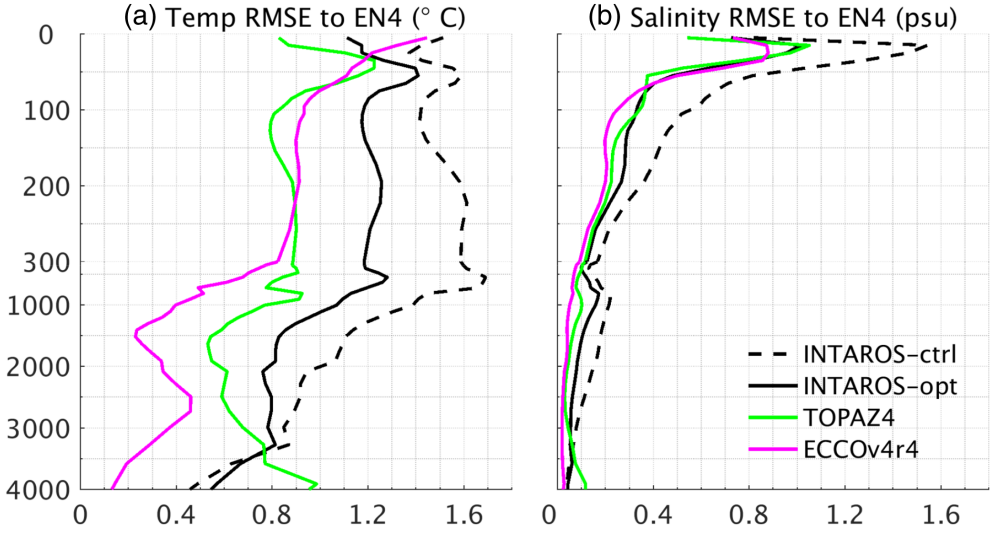

FIGURE 7 RMS differences of (a) temperature and (b) salinity in INTAROS-ctrl, INTAROS-opt, TOPAZ4, and ECCOV4r4 to the profile data [Colour figure can be viewed at wileyonlinelibrary.com]

especially in the Arctic Ocean and the Greenland and Iceland seas. The ratio of error reduction (Figure 8c) reveals that temperature errors are reduced by 40–80% in the central model domain. Degradations are visible in the southern boundary in the Atlantic section, where the boundary condition likely dominates temperature changes.

TOPAZ4 (Figure 8d) and ECCOv4r4 (Figure 8e) show smaller temperature errors, especially in the deep basin. Besides, ECCOv4r4 shows the smallest temperature errors in the Greenland, Iceland, and Norwegian seas. The water is then transported into the Arctic Ocean, resulting in the smallest temperature errors of the Arctic Atlantic water.

Salinity differences to profile observations are shown in Figure 9 to illustrate salinity errors of the four simulations in the top 100 m. INTAROS-ctrl (Figure 9a) is saltier in the western Canadian Basin and the Labrador Sea and is fresher in the Eurasian Basin and the north Atlantic Ocean. Upon data assimilation, salinity errors are reduced in most regions (Figure 9b). The ratio of salinity error reduction (Figure 9c) shows an overall improvement of salinity in most model domains, but degradations also occur occasionally. TOPAZ4 simulates a fresher Arctic Ocean with salinity errors up to −0.8 psu (Figure 9d) and smaller salinity errors in the Atlantic section (Figure 9d) except near the coast. ECCOv4r4 (Figure 9e) also shows small salinity errors in the Atlantic section, but the errors remain large in the Arctic Ocean.

5.2 | SST changes

SST is consistent among the Arctic ocean–sea ice reanalyses (Chevallier *et al.*, 2017) and interacts with sea ice directly. We compare the mean SST difference and RMSEs of SST anomaly between the four simulations and RSS-SST.

In INTAROS-ctrl, the mean SST (Figure 10a) shows strong cold biases up to −3 °C and SST anomaly (Figure 10b) also show significant errors, especially in seasonal sea ice extent regions. Upon data assimilation, INTAROS-opt reduces the mean SST biases up to 2 °C in large areas of the pan-Arctic Ocean (Figure 10c). Reduction of RMSEs of SST anomaly (Figure 10d) up to 1 °C is also achieved.

TOPAZ4 shows slightly smaller SST errors regarding the mean SST (Figure 10e) and SST anomaly (Figure 10f), especially in the marginals seas and around Greenland. ECCOv4r4 shows the largest cold biases (Figure 10g) and RMSEs of SST anomaly (Figure 10h) in the pan-Arctic Ocean, which is likely caused by the misrepresentation of the sea ice processes.

In all the simulations, SST differences of the mean state and of the variability remain along the strong currents and the variable ice extent regions. We take the SST time series (Figure 11c) averaged over a 50 × 50 km box near Fram Strait (green box in Figure 10b) as an example to examine and explain the differences between the reanalyses and observations. During September–November 2012, SIC observations averaged over this box (blue line in Figure 11b) show sea ice appearing from September 27 to October 26, accompanied by declining SST (Figure 11c). Both INTAROS-opt and TOPAZ4 (black and green lines in Figure 11b, c) simulate a similar process as the observations, starting from October 11 to October 23 and September 27 to November 23, respectively. Based on INTAROS-opt, we diagnose SIC changes ($\Delta \boldsymbol{A}$) due to sea ice advective divergence ($-\boldsymbol{\nabla} \cdot (\vec{\boldsymbol{u}}\boldsymbol{A})$, $\boldsymbol{S}_{\mathbf{div}}$), atmospheric thermodynamic effects ($\boldsymbol{S}_{\mathbf{atm}}$), and oceanic thermodynamic effects ($\boldsymbol{S}_{\mathbf{oce}}$, Figure 11a). Figure 11a reveals that the advective divergence effect dominates the accumulation of sea ice in this region. The underlying water cools as the ice is moving in. It melts the ice from underneath,

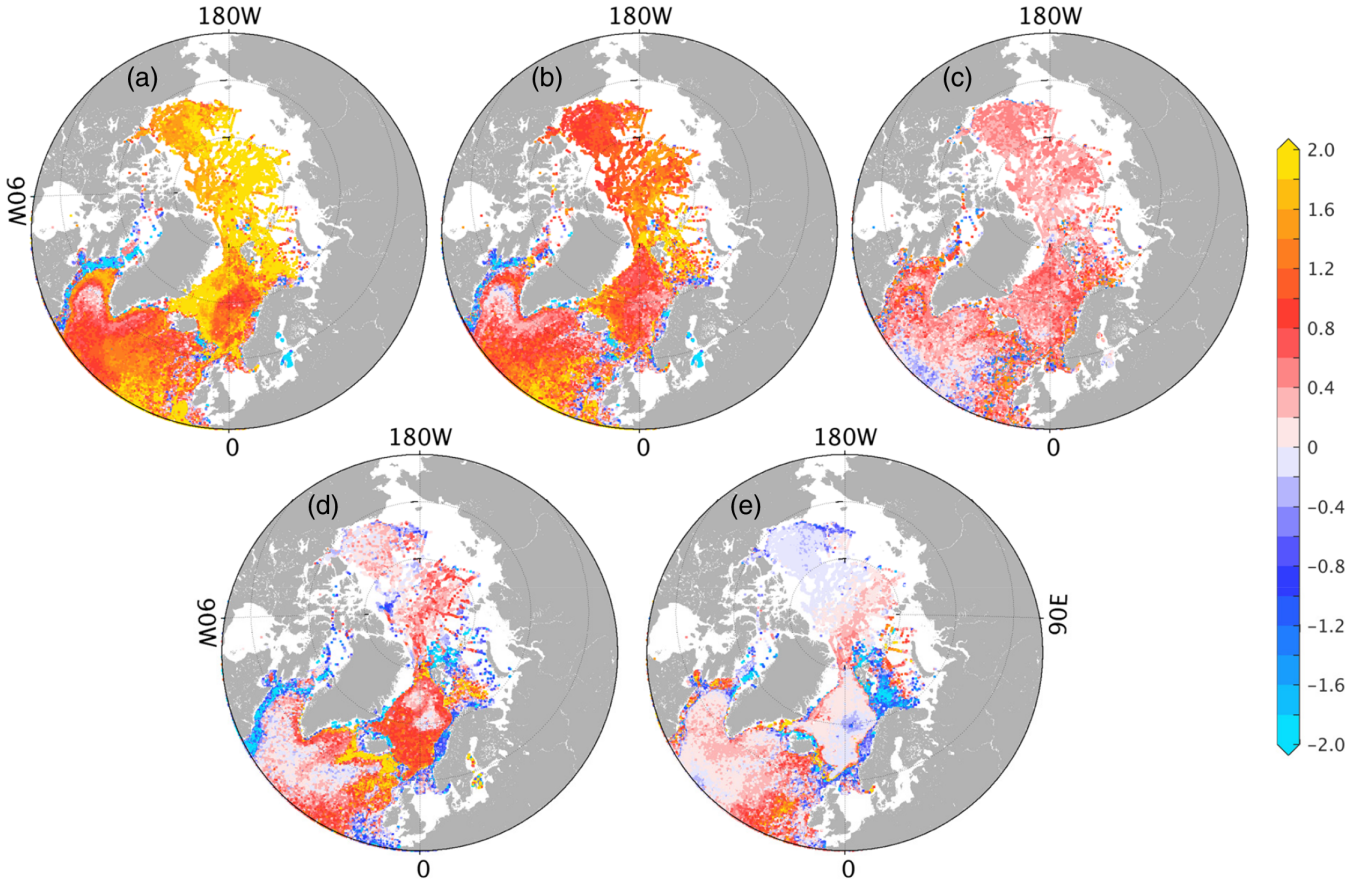

FIGURE 8 Potential temperature differences in (a) INTAROS-ctrl, (b) INTAROS-opt, (d) TOPAZ4, and (e) ECCOv4r4 to EN4 data in the layer 100–1,000 m. Panel (c) is the ratio of potential temperature error reduction upon data assimilation [Colour figure can be viewed at wileyonlinelibrary.com]

shown by the negative contribution from the oceanic thermodynamic effect. The small contributions from the thermodynamics suggest that the colder water moves together with the ice into the box, while surface fluxes have a minor impact. In TOPAZ4 (green lines in Figure 11b,c), sea ice emerges at a date similar to SIC observations, but more sea ice is simulated in the middle of October. During the decay, SIC is reduced (corrected) during each step (every 7 days) of the data assimilation before building up biases again between two analysis cycles. In general, no dynamics can be inferred behind the SIC changes. The decay process in the TOPAZ4 reanalysis takes more time. In contrast, INTAROS-ctrl and ECCOv4r4 fail to reproduce this sea ice intrusion process, and therefore, significant SST errors remain in these two simulations.

We conclude that, overall, the adjoint method improves both the variability and the mean state of the SST. INTAROS-opt is consistent with TOPAZ4 in general, but SST differences remain along sea ice extent regions and strong current regions, related to the fast ocean–sea ice interaction processes.

5.3 | Freshwater content

In this section, we examine freshwater content (referred to 34.8 psu as in Proshutinsky *et al.*, 2009) in INTAROS-opt, TOPAZ4, and ECCOv4r4, and take freshwater content in the Beaufort Sea and the Laptev and the East Siberian seas as examples to examine their mean values and variability.

After the assimilation, a freshening is noticeable in the interior of the Arctic Ocean (Figure 12a). At the same time, along the routes of outflowing Arctic water into the North Atlantic east and west of Greenland, a reduction of freshwater content can be seen. Circulation changes (vectors in Figure 12a) depict an enhanced anticyclonic circulation anomaly in the Canadian Basin and a weaker anticyclonic circulation anomaly in the Eurasian Basin. We also note an increase of Atlantic inflow west of Svalbard and St. Anna Trough and enhanced Arctic outflow through the western Fram Strait and Nares Strait. The freshwater comes mostly from the direct adjustment of the initial salinity of the year 2007 (Figure 12b). It is then redistributed towards the Canadian Basin via the mean circulation. The enhanced

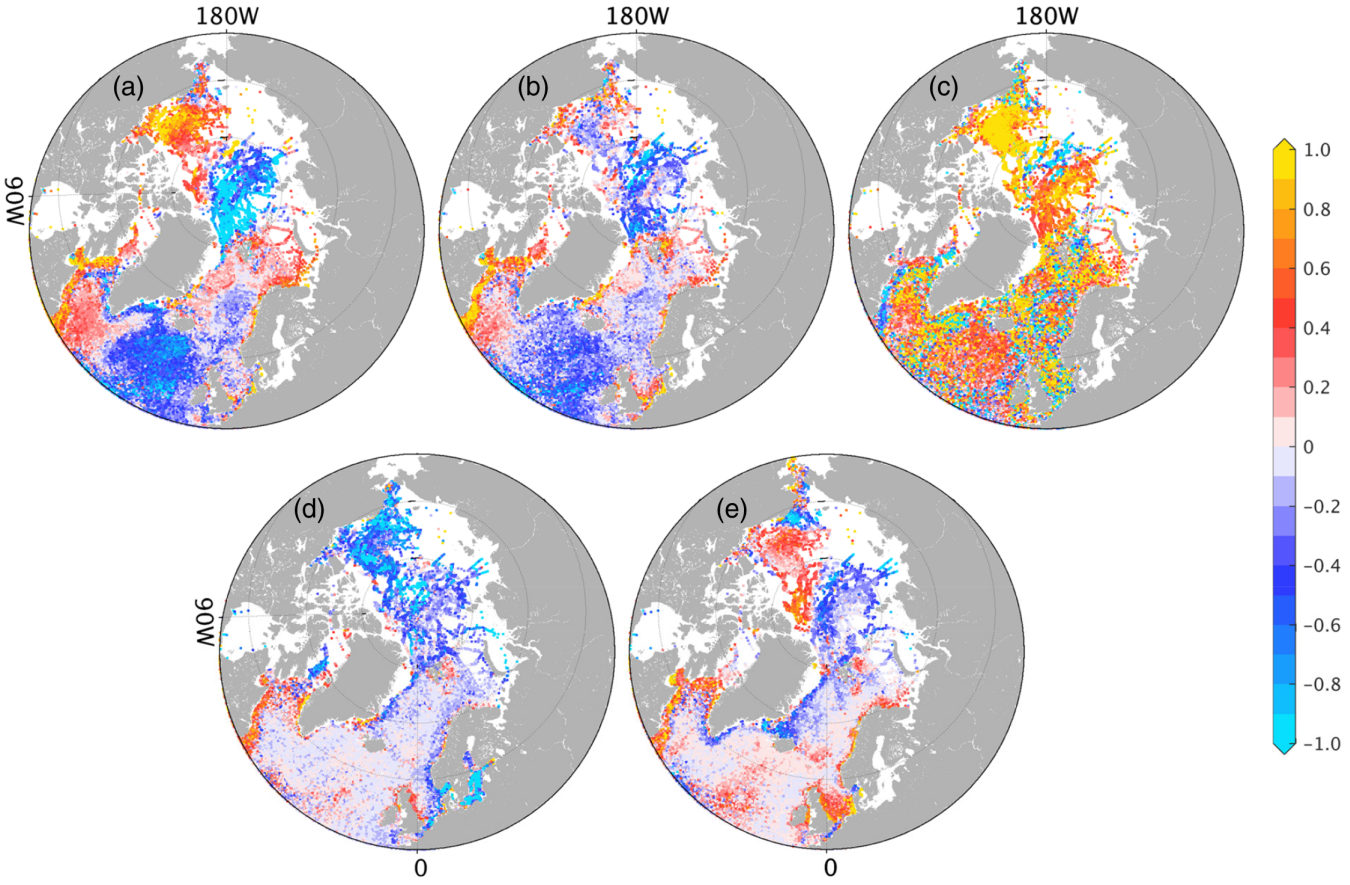

FIGURE 9 Salinity differences in (a) INTAROS-ctrl, (b) INTAROS-opt, (d) TOPAZ4, and (e) ECCOv4r4 to EN4 data in the top 100 m. Panel (c) is the ratio of salinity error reduction upon data assimilation [Colour figure can be viewed at wileyonlinelibrary.com]

circulation around Greenland would, according to Köhl and Serra (2014), contribute to the reduction of the freshwater content. The additional freshwater content remains in the Canadian Basin through the enhanced anticyclonic circulation, as revealed by Morison *et al.* (2012).

Compared with TOPAZ4 and ECCOv4r4, INTAROS-opt simulates less freshwater content over the Arctic continental shelves and slightly more freshwater in the Canadian Basin (Figure 13a,b). One may argue that INTAROS-opt increases the freshwater content in the Canadian Basin at the expense of degrading the Arctic continental shelves. However, the mean freshwater content increment after data assimilation (Figure 13a) shows almost no changes in the Arctic marginal seas.

Based on annual observations (Proshutinsky *et al.*, 2009; 2019), the WOA18 atlas (Zweng *et al.*, 2018), the PHC atlas version 3.0 (Steele *et al.*, 2001), INTAROS-opt, TOPAZ4, and ECCOv4r4, we computed the freshwater content in the Beaufort Sea (Figure 13c) and the Laptev and East Siberian seas (Figure 13d). INTAROS-opt changes the mean freshwater content without altering its variability significantly. The mean freshwater content in the Beaufort Sea is increased from 12 to 16 km^3 after data assimilation (Figure 13c), and changes in the marginal seas are also visible (Figure 13d).

Freshwater content remains different in TOPAZ4, INTAROS-opt, and ECCOv4r4 (Figure 13a,b), especially over the Arctic marginal shelves. In TOPAZ4, sea surface salinity (SSS) is relaxed to a combined climatology of the WOA05 and the version 3.0 of Polar science center Hydrographic Climatology (PHC, Steele *et al.*, 2001) with a timescale of 30 days to complement limitations of seasonal river discharge and relatively coarse atmospheric forcing. In INTAROS-opt and ECCOv4r4, the salinity is mainly changed by adjustment of initial salinity and atmospheric forcing. The SSS restoring term seems more efficient in changing SSS than adjusting atmospheric forcing in the marginal seas. However, salinity relaxation dampens the seasonal freshwater content variability (green lines in Figure 13c,d).

In this study, the WOA18 data remain an essential source of hydrographic observations to constrain the model's climatology. However, the differences between different hydrographic atlases remain significant (Figure 13c,d), caused by different sources of observations and temporal coverage of the Arctic Ocean atlas. The PHC

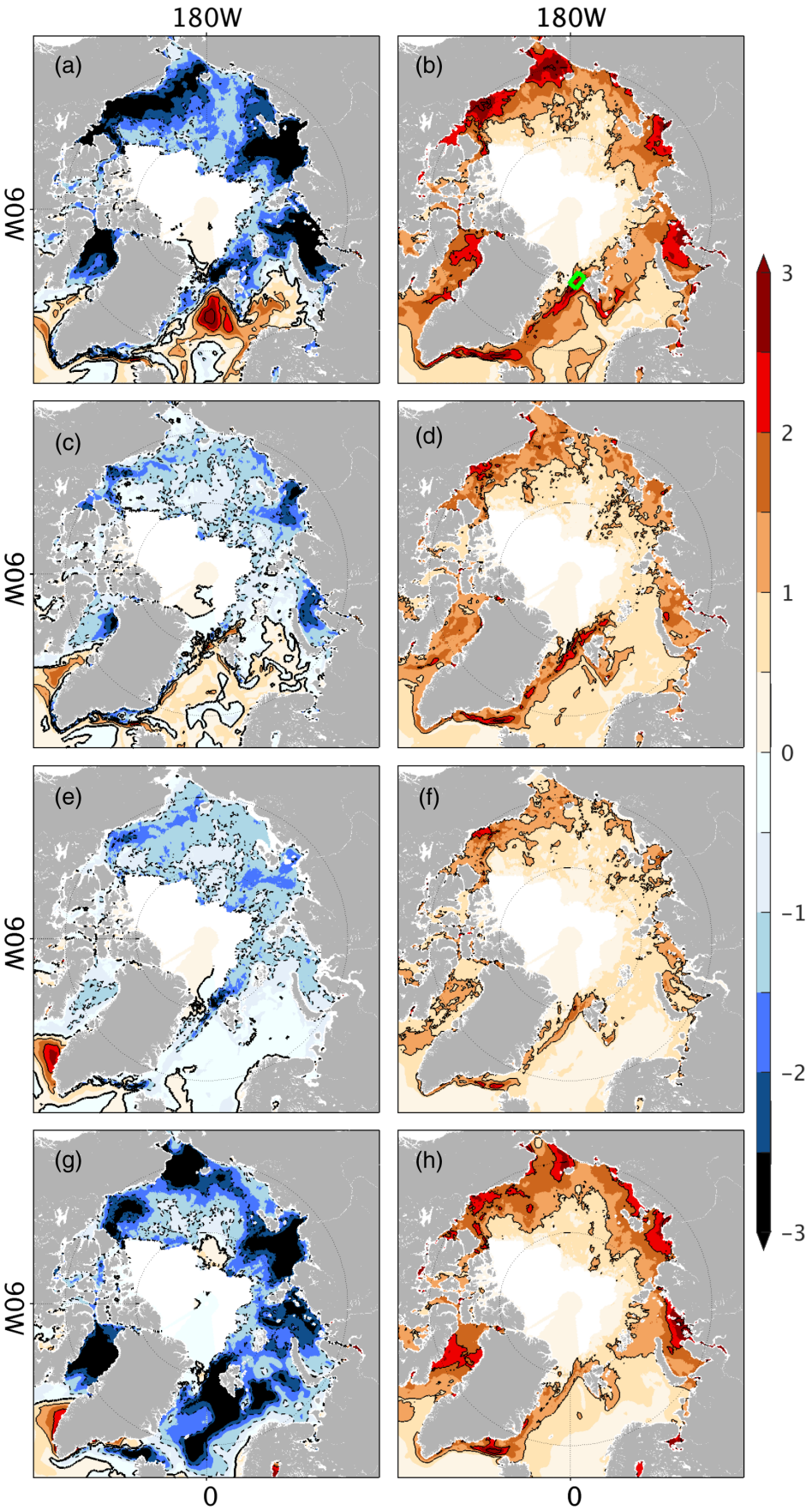

FIGURE 10 Mean SST difference to RSS-SST in (a) INTAROS-ctrl, (c) INTAROS-opt, (e) TOPAZ4, and (g) ECCOv4r4. The right column is the corresponding root mean square difference between the temporal anomalies of SST of the four simulations and those of RSS-SST. The contour interval is 1 °C, and the green box indicates regions that are used in Figure 11 below [Colour figure can be viewed at wileyonlinelibrary.com]

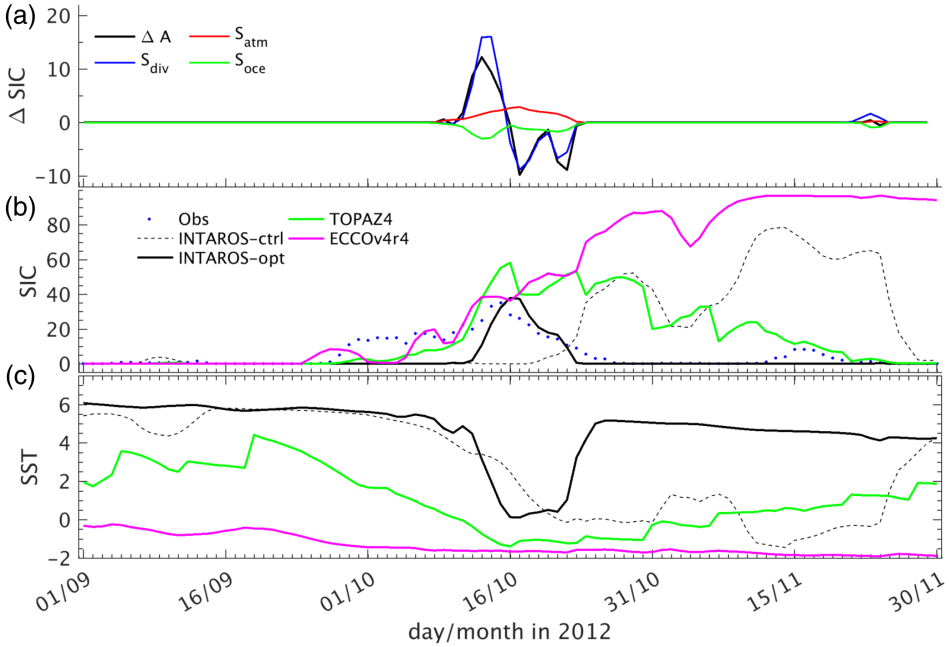

FIGURE 11 (a) Time series of SIC changes ($\boldsymbol{\Delta A}$) for the region near the Fram Strait (green box in Figure 10b) from September 1, 2012, to November 30, 2012, and attributions to oceanic ($\boldsymbol{S_{oce}}$) and atmospheric ($\boldsymbol{S_{atm}}$) thermodynamic effects, and sea ice advective divergence term ($\boldsymbol{S_{div}}$) on SIC changes ($\boldsymbol{\Delta A}$). Individual terms are diagnosed with INTAROS-opt. Panels (b),(c) are time series of SIC and SST for the same region from observations and the four simulations (see legend in panel (b)) [Colour figure can be viewed at wileyonlinelibrary.com]

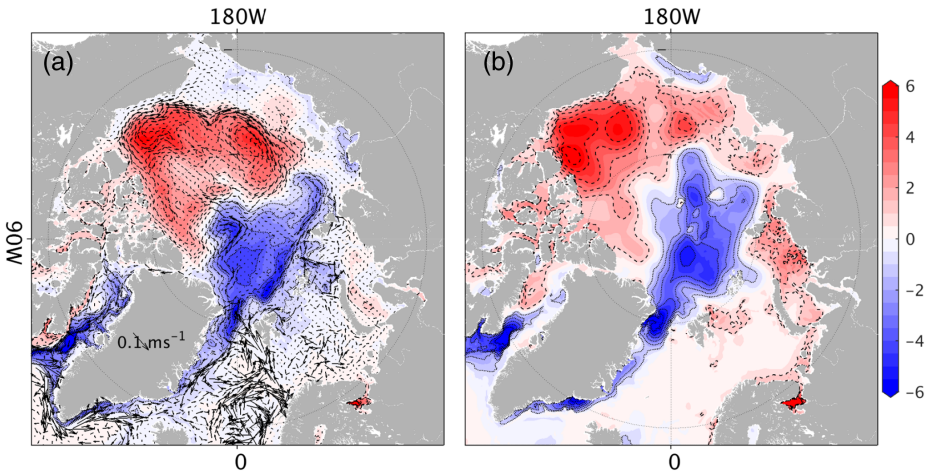

FIGURE 12 (a) Difference in mean freshwater content (in meters, shading) and velocity in the top 100 m (vectors) between INTAROS-opt and INTAROS-ctrl. Panel (b) shows the freshwater content increment introduced by the initial salinity adjustment. The contour interval is 1 m [Colour figure can be viewed at wileyonlinelibrary.com]

atlas data merge WOA98 with the regional Arctic Ocean atlas, providing a good description of the Arctic Ocean before the 2000s (Steele *et al.*, 2001). In contrast, WOA18 data include observations until 2018, but may not include all data from the regional atlas. Therefore, improving the quality of the Arctic Ocean climatology is required to further reduce the model-simulated salinity biases through data assimilation.

5.4 | Oceanic and sea ice volume transports

The Arctic freshwater content and transports through the key straits remain different among Arctic ocean models and reanalyses (Aksenov *et al.*, 2016; Uotila *et al.*, 2019). In contrast to Koldunov *et al.* (2017), our results show that the assimilation changes the ocean circulation in the pan-Arctic Ocean (Figure 13a). We examine the transport changes in detail. Table 3 presents mean fluxes of volume, liquid freshwater, sea ice volume, and heat through the Fram Strait, Davis Strait, and the Barents Sea Opening in INTAROS-ctrl and INTAROS-opt.

As can be seen, changes in the fluxes are more significant than those shown by Koldunov *et al.* (2017). Sea ice volume transports are reduced by ~26.4% through the Barents Sea Opening while increased by 30.9% through the Fram Strait. Net southward volume flux through the Fram Strait is reduced by 16.8% because of an enhancement of the Norwegian North Atlantic Current and a weakening of the Arctic outflow, resulting in increased heat fluxes to the Arctic Ocean and decreased freshwater flux from the Arctic Ocean. The southward net volume flux through the Davis Strait is increased, accompanied by

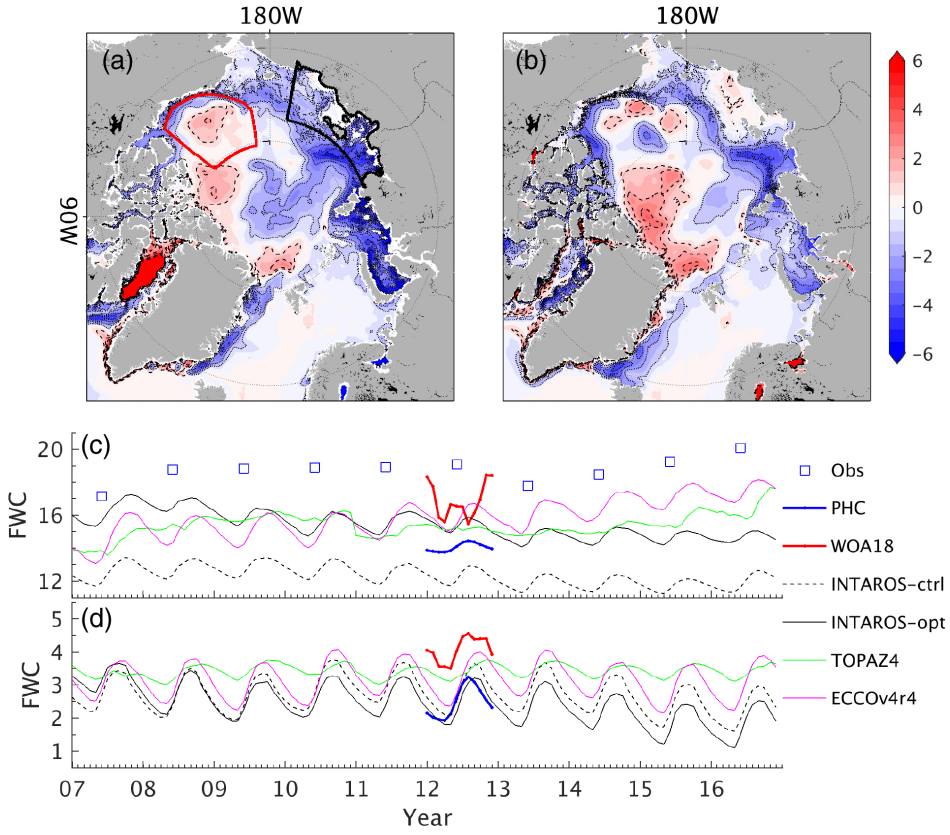

FIGURE 13 Differences in freshwater content (in meters) between INTAROS-opt and (a) TOPAZ4 or (b) ECCOv4r4. Panels (c) and (d) are the accumulated freshwater content ($\times 10^3$ km^3) in the Beaufort Sea (enclosed by the red line in panel (a)), and in the Laptev and the East Siberian seas (enclosed by the black line in panel (b)) based on INTAROS-ctrl, the three reanalyses, the PHC3.0, and WOA18 climatology (see legend). Observed freshwater content in the Beaufort Gyre (blue squares, https://www.whoi.edu/website/beaufortgyre/data) is also overlaid in panel (c) [Colour figure can be viewed at wileyonlinelibrary.com]

TABLE 3 Mean volume flux (VF, in Sv), liquid freshwater flux (LFWF, in mSv), sea ice volume transport (SIVF, in mSv), and heat flux (HF, in TW) through the Fram Strait (FS), Davis Strait (DS), and Barents Sea Opening (BSO) in INTAROS-ctrl and INTAROS-opt, their difference in %, and from the observational estimates. Significant changes (>10% or <-10%) are in bold.

		INTAROS-ctrl	INTAROS-opt	Difference (%)	Obs
BSO	VF	2.8	2.9	1.3	1.8[a]
	LFWF	−2.1	−2.0	−4.8	NA
	SIVF	−3.1	−1.0	**−26.4**	NA
	HF	83.7	76.1	−9.1	48.0[a]
Davis	VF	−0.5	−1.1	**109.7**	-1.6 ± 0.5[b]
	LFWF	−15.3	−49.1	**220.6**	-93.0 ± 6.0[b]
	SIVT	−11.5	−11.2	−1.9	-10.0 ± 1.0[b]
	HF	10.9	11.9	8.0	20.0 ± 9.0[b]
Fram	VF	−3.3	−2.7	**−16.8**	-1.8 ± 5.0[c]
	LFWF	−70.8	−42.5	**−40.0**	-84.3 ± 16.7[c]
	SIVT	−50.1	−56.4	**30.9**	70.0[d]
	HF	37.3	39.0	4.6	NA

[a]1998–2006 Average (Skagseth *et al.*, 2008).
[b]2004–2010 Average (Curry *et al.*, 2014), the estimates vary depending on different years (Cuny et al., 2005; 2011).
[c]Based on moorings covering different periods (Schauer *et al.*, 2008; de Steur *et al.*, 2009; Fieg *et al.*, 2010).
[d]1991–1998 average (Kwok *et al.*, 2004).

more southward freshwater transport. Data assimilation does not always bring oceanic transport closer to observations, as the reduced liquid freshwater flux through the Fram Strait shows. Unfortunately, direct observations of the transports through the key straits cover different periods. Particular methods are used to fill the spatial gaps,

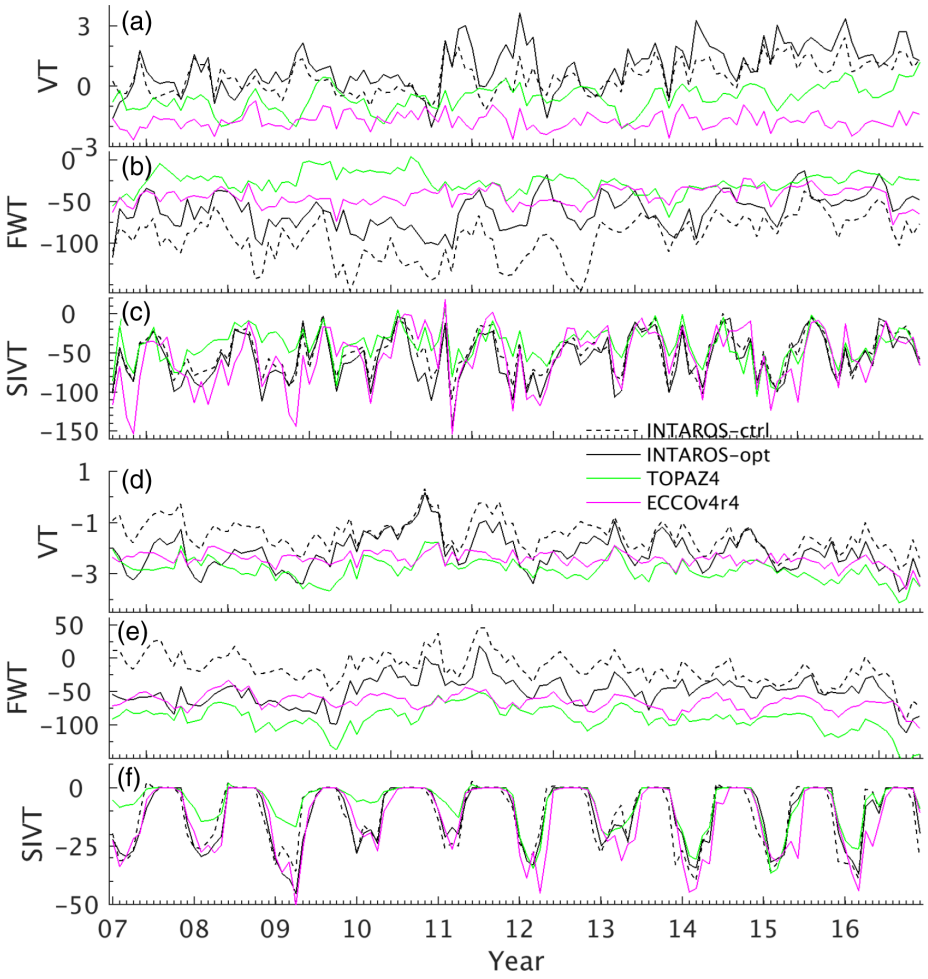

FIGURE 14 Volume (in Sv), liquid freshwater (in mSv), and sea ice volume (in mSv) transports through the (a–c) Fram Strait and (d–f) Davis Strait in the four simulations. The volume and liquid freshwater flux are computed over the top 500 m [Colour figure can be viewed at wileyonlinelibrary.com]

resulting in significant uncertainties in the observational estimates. Moreover, model studies (Köhl and Serra, 2014) also show substantial decadal variability of the transports. Because of this, direct comparisons are complicated, and conclusions drawn could be ambiguous.

The time series of volume, liquid freshwater, and sea ice volume transports from INTAROS-ctrl, INTAROS-opt, TOPAZ4, and ECCOv4r4 is shown in Figure 14. Upon data assimilation, mean freshwater transports through the Fram Strait (Figure 14b) and the Davis Strait (Figure 14e) are substantially changed, but the variability changes are small. A better match of sea ice volume transport (Figure 14c,f) is observed in the three reanalyses than for the liquid freshwater transport (Figure 14b,e) and volume transport (Figure 14a,d), especially after the year 2012. Regardless of the biases, the variability of volume and liquid freshwater transport through the Davis Strait matches well in TOPAZ4, ECCOv4r4, and INTAROS-opt (Figure 14d,e). However, no clear correlations are observed in volume and liquid freshwater transports through the Fram Strait (Figure 14a,b).

Overall, the optimization changes the mean freshwater transports through the Fram Strait and the Davis Strait. However, the mean volume and liquid freshwater fluxes through the key straits remain different in the three reanalyses.

6 | ADJUSTMENTS OF THE CONTROL VARIABLES

Unique to our optimization is that corrections to the control variables are the only means for adjusting the model to reduce the model–data misfit while leaving the model dynamics untouched. Figure 15a shows the resulting normalized adjustments of atmospheric states averaged over the model domain. Changes of the atmospheric state in the first 4-year period are smaller than in the remaining years, caused by a low number of iterations in this segment and the additional option to adjust the initial state in the year 2007. Because more iterations have been performed, corrections to the atmospheric forcing are more pronounced than those shown in the study of Koldunov *et al.* (2017).

Among all atmospheric states, wind components are adjusted most noticeably by the optimization algorithm. The 2-m air temperature and specific humidity are also

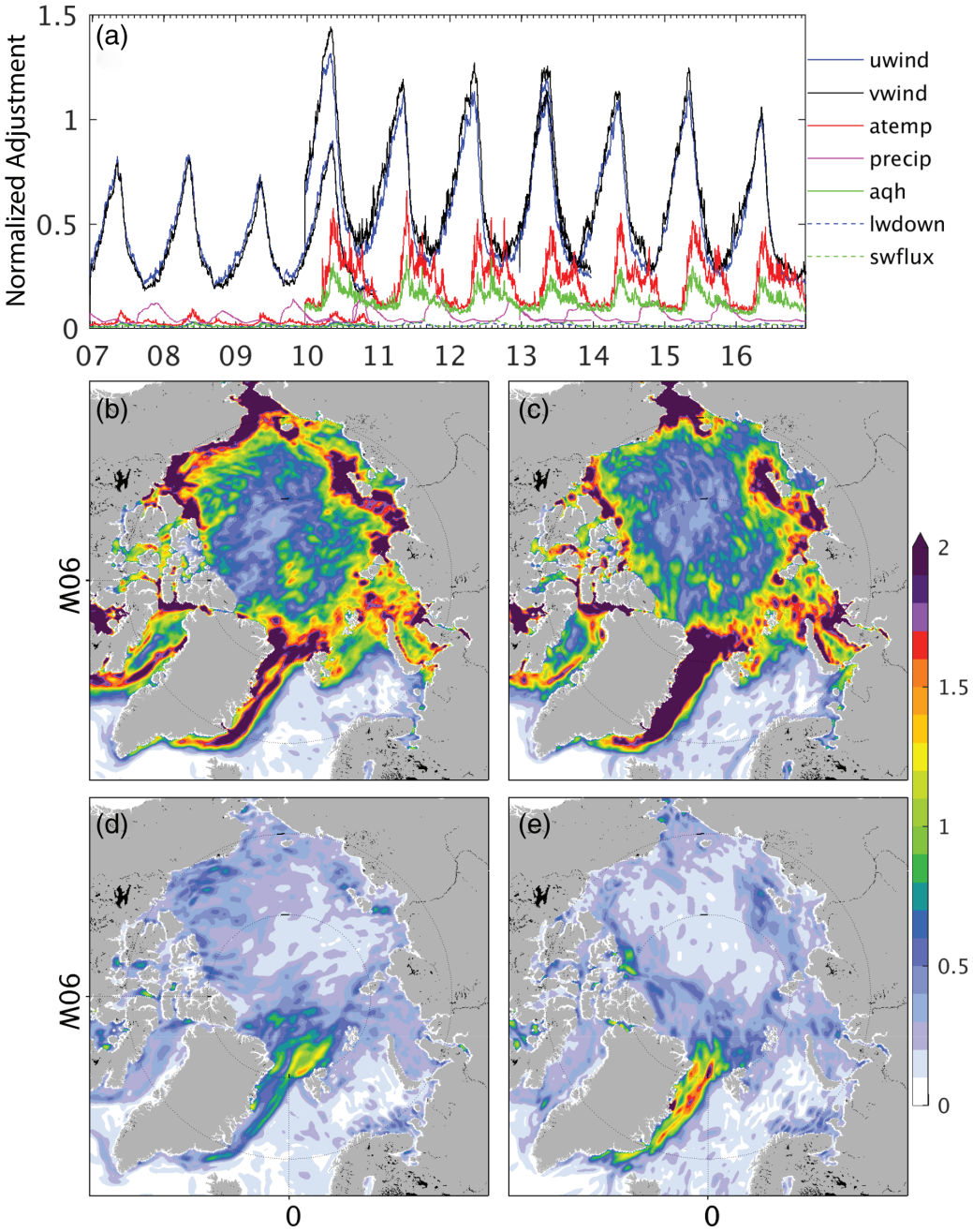

FIGURE 15 (a) Area average of the adjustments of the control variables (see legend) normalized by their uncertainties. Adjustments of the overlapping years (2010 and 2013) are also shown. Panels (b, c) are normalized root mean square of corrections to (b) wind *u*-component anomaly, (c) wind *v*-component anomaly in May. Panels (d, e) are similar to (b, c) but for November [Colour figure can be viewed at wileyonlinelibrary.com]

substantially changed; their adjustments are still smaller than those of the wind. During the winter season, wind components seem to be the most efficient control variables because the Arctic Ocean is covered by sea ice blocking the heat and freshwater fluxes between the ocean and atmosphere. Although the same applies to the transfer of momentum, the free drift approximation in the adjoint enables the transfer of corrections to the wind, which is likely to be much less efficient than what the adjoint predicts. From April to October, the roles of 2-m air temperature and specific humidity increase because of more open water.

We focus on corrections of the wind vectors in May (Figure 15b,c) and November (Figure 15e,f) when the corrections are at the maximum and minimum, respectively. Normalized root mean squares of *u* and *v* wind correction anomalies depict substantial adjustments of wind vectors over seasonal sea ice extent regions in May (Figure 15b,c)

and along the East Greenland Current (Figure 15e,f). Wind vectors in May are one of the most crucial factors that impact SIC in September (Kauker *et al.*, 2009), indicating that wind vectors likely impact the SIC several months later through sea ice advective convergence effects. Therefore, corrections to wind vectors in May and November may change SIC over the seasonal sea ice extent region months later.

7 | CONCLUSIONS

Building on the work of Koldunov *et al.* (2017), we provide here an Arctic ocean–sea ice reanalysis for the period 2007–2016. By applying a filter algorithm to the adjoint sensitivities, thereby eliminating local random spikes in the respective fields, we increased both the assimilation window (to 4 years) and the number of iterations performed over each window. Through the filter process, the adjoint model may underestimate the real sensitivities of the cost function to control parameters related to ocean–sea ice processes (Appendix). Nevertheless, remaining adjoint sensitivities appear still effective during the optimization process in reducing the model–data misfits. The optimization achieves a significantly larger cost function reduction, through the increased number of iterations, than reported previously by Koldunov *et al.* (2017). The data assimilation approach improves the spatial sea ice distribution and reduces total SIA in the winter season. Together with SIC, SST is also significantly improved. However, despite the significant improvement in SIT estimates, we note that residual SIT and sea ice volume errors remain substantial.

INTAROS-opt, TOPAZ4, and PIOMAS reproduce the SIC variations well. In contrast, ECCOv4r4 fails to reproduce SIC correctly because of the exclusion of the adjoint of the sea ice model. SIT differences between different reanalyses remain large, with INTAROS-opt and TOPAZ4 showing smaller RMSEs (0.40 and 0.41 m, respectively) than that in PIOMAS and ECCOv4r4 (0.46 and 0.52 m, respectively).

Temperature and salinity errors are also reduced upon assimilating WOA18 and hydrographic profile observations. However, large temperature and salinity errors remain in INTAROS-opt in the Atlantic sector. We speculate that the large errors, especially the temperature biases in the intermediate layer, are related to the biased boundary conditions, which are not adjusted in our study. Discrepancies in the freshwater content and transports across the Fram and Davis straits remain large between different reanalyses, supporting the need to improve coverage of hydrographic observations in the Arctic Ocean.

Compared with the other filter-based ocean–sea ice reanalyses, our product is dynamically consistent and reproduces the sea ice parameters and the underlying ocean state well. The data could be used for understanding the causes and consequences of the Arctic sea ice changes. The results above encourage us to use, in future applications, a single assimilation window, adjust the boundary conditions, and extend the reanalysis from the year 1991 to now.

ACKNOWLEDGMENTS

This work was supported partly through funding received from project INTAROS, funded by the European Union (Grant 727890). We thank NCEP for offering the NCEP/NCAR-RA1 atmosphere reanalysis data (https://psl.noaa.gov/). The PIOMAS reanalysis is derived from http://psc.apl.uw.edu/research/projects/arctic-sea-ice-volume-anomaly/data/, the TOPAZ4 reanalysis is from http://my.cmems-du.eu/Core/ARCTIC_REANALYSIS_PHYS_002_003/dataset-ran-arc-day-myocean v2-be/, and ECCOv4r4 is from https://ecco-group.org/products-ECCO-V4r4.htm. We thank BGEP (https://www.whoi.edu/page.do?pid=66559) and NABOS (https://uaf-iarc.org/nabos/) for sharing in situ profiles and mooring observations. Hydrographic profiles are extracted from EN4 (https://www.metoffice.gov.uk/hadobs/en4/) and UDASH (https://pangaea.de/10.1594/PANGAEA.872931) databases. The along-track SLA data is derived from C3S (https://climate.copernicus.eu/). The ocean–sea ice reanalysis presented here is available at https://catalog-intaros.nersc.no/dataset/ocean-sea-ice-synthesis-from-2007-2016. The model simulations were performed at the Deutsches Klimarechenzentrum (DKRZ), Hamburg, Germany. Contribution to the DFG funded Excellence Cluster CLICCS at the Center for Earth System Research and Sustainability of the University of Hamburg. We thank two anonymous reviewers for their constructive and detailed comments that helped us to greatly improve the manuscript.

ORCID

Guokun Lyu https://orcid.org/0000-0003-0079-5352
Armin Koehl https://orcid.org/0000-0002-9777-674X
Jiping Xie https://orcid.org/0000-0002-8602-2774

REFERENCES

Aksenov, Y., Karcher, M., Proshutinsky, A., Gerdes, R., De Cuevas, B., Golubeva, E., Kauker, F., Nguyen, A.T., Platov, G.A. and Wadley, M. (2016) Arctic pathways of Pacific water: Arctic Ocean model intercomparison experiments. *Journal of Geophysical Research: Oceans*, 121, 27–59.

AMAP. (2019) *AMAP Climate Change Update 2019: An Update to Key Findings of Snow, Water, Ice and Permafrost in the Arctic*

(SWIPA) 2017. Oslo: Arctic Monitoring and Assessment Programme (AMAP), 1–12.

Armitage, T.W., Bacon, S., Ridout, A.L., Thomas, S.F., Aksenov, Y. and Wingham, D.J. (2016) Arctic Sea surface height variability and change from satellite radar altimetry and GRACE, 2003–2014. *Journal of Geophysical Research: Oceans*, 121, 4303–4322.

Behrendt, A., Sumata, H., Rabe, B. and Schauer, U. (2018) UDASH – unified database for Arctic and subarctic hydrography. *Earth System Science Data*, 10, 1119–1138.

Chevallier, M., Smith, G.C., Dupont, F., Lemieux, J.-F., Forget, G., Fujii, Y., Hernandez, F., Msadek, R., Peterson, K.A., Storto, A., Toyoda, T., Valdivieso, M., Vernieres, G., Zuo, H., Balmaseda, M., Chang, Y.-S., Ferry, N., Garric, G., Haines, K., Keeley, S., Kovach, R.M., Kuragano, T., Masina, S., Tang, Y., Tsujino, H. and Wang, X. (2017) Intercomparison of the Arctic Sea ice cover in global ocean–sea ice reanalyses from the ORA-IP project. *Climate Dynamics*, 49, 1107–1136.

Cuny, J., Rhines, P.B. and Kwok, R. (2005) Davis Strait volume, freshwater and heat fluxes. *Deep Sea Research Part I: Oceanographic Research*, 52, 519–542.

Curry, B., Lee, C. and Petrie, B. (2011) Volume, freshwater, and heat fluxes through Davis Strait, 2004–05. *Journal of Physical Oceanography*, 41, 429–436.

Curry, B., Lee, C.M., Petrie, B., Moritz, R.E. and Kwok, R. (2014) Multiyear volume, liquid freshwater, and sea ice transports through Davis Strait, 2004–10. *Journal of Physical Oceanography*, 44, 1244–1266.

de Steur, L., Hansen, E., Gerdes, R., Karcher, M., Fahrbach, E. and Holfort, J. (2009) Freshwater fluxes in the East Greenland current: a decade of observations. *Geophysical Research Letters*, 36, L23611.

Dmitrenko, I.A., Polyakov, I.V., Kirillov, S.A., Timokhov, L.A., Frolov, I.E., Sokolov, V.T., Simmons, H.L., Ivanov, V.V. and Walsh, D. (2008) Toward a warmer Arctic Ocean: spreading of the early 21st century Atlantic water warm anomaly along the Eurasian Basin margins. *Journal of Geophysical Research: Oceans*, 113, C05023.

ECCO Consortium, Fukumori, I., Wang, O., Fenty, I., Forget, G., Heimbach, P. and Ponte, R. M. (2020a). ECCO Central Estimate (Version 4 Release 4).

ECCO Consortium, Fukumori, I., Wang, O., Fenty, I., Forget, G., Heimbach, P. and Ponte, R. M. (2020b). Synopsis of the ECCO Central Production Global Ocean and Sea-Ice State Estimate (Version 4 Release 4).

Fenty, I. and Heimbach, P. (2013) Coupled sea ice–ocean-state estimation in the Labrador Sea and Baffin Bay. *Journal of Physical Oceanography*, 43, 884–904.

Fenty, I., Menemenlis, D. and Zhang, H. (2017) Global coupled sea ice-ocean state estimation. *Climate Dynamics*, 49, 931–956.

Fieg, K., Gerdes, R., Fahrbach, E., Beszczynska-Möller, A. and Schauer, U. (2010) Simulation of oceanic volume transports through Fram Strait 1995–2005. *Ocean Dynamics*, 60, 491–502.

Forget, G., Campin, J.M., Heimbach, P., Hill, C.N., Ponte, R.M. and Wunsch, C. (2015) ECCO version 4: an integrated framework for non-linear inverse modeling and global ocean state estimation. *Geoscientific Model Development*, 8, 3071–3104.

Giering, R. and Kaminski, T. (1998) Recipes for adjoint code construction. *ACM Transactions on Mathematical Software (TOMS)*, 24, 437–474.

Gilbert, J. C. and Lemaréchal, C. (2006). The module M1QN3.

Good, S.A., Martin, M.J. and Rayner, N.A. (2013) EN4: quality controlled ocean temperature and salinity profiles and monthly objective analyses with uncertainty estimates. *Journal of Geophysical Research: Oceans*, 118, 6704–6716.

Heimbach, P., Menemenlis, D., Losch, M., Campin, J.-M. and Hill, C. (2010) On the formulation of sea-ice models. Part 2: lessons from multi-year adjoint sea-ice export sensitivities through the Canadian Arctic archipelago. *Ocean Modelling*, 33, 145–158.

Hibler, W. (1979) A dynamic thermodynamic sea ice model. *Journal of Physical Oceanography*, 9, 815–846.

Hibler, W. (1980) Modeling a variable thickness sea ice cover. *Monthly Weather Review*, 108, 1943–1973.

Kaleschke, L., Lüpkes, C., Vihma, T., Haarpaintner, J., Bochert, A., Hartmann, J. and Heygster, G. (2001) SSM/I sea ice remote sensing for mesoscale ocean-atmosphere interaction analysis. *Canadian Journal of Remote Sensing*, 27, 526–537.

Kalnay, E., Kanamitsu, M., Kistler, R., Collins, W., Deaven, D., Gandin, L., Iredell, M., Saha, S., White, G. and Woollen, J. (1996) The NCEP/NCAR 40-year reanalysis project. *Bulletin of the American Meteorological Society*, 77, 437–471.

Kauker, F., Kaminski, T., Karcher, M., Giering, R., Gerdes, R. and Voßbeck, M. (2009) Adjoint analysis of the 2007 all time Arctic sea-ice minimum. *Geophysical Research Letters*, 36, L03707.

Köhl, A. (2015) Evaluation of the GECCO2 ocean synthesis: transports of volume, heat and freshwater in the Atlantic. *Quarterly Journal of the Royal Meteorological Society*, 141, 166–181.

Köhl, A. and Serra, N. (2014) Causes of decadal changes of the freshwater content in the Arctic Ocean. *Journal of Climate*, 27, 3461–3475.

Koldunov, N.V., Köhl, A., Serra, N. and Stammer, D. (2017) Sea ice assimilation into a coupled ocean–sea ice model using its adjoint. *The Cryosphere*, 11, 2265–2281.

Kwok, R. (2018) Arctic sea ice thickness, volume, and multiyear ice coverage: losses and coupled variability (1958–2018). *Environmental Research Letters*, 13, 105005.

Kwok, R., Cunningham, G.F. and Pang, S.S. (2004) Fram Strait sea ice outflow. *Journal of Geophysical Research: Oceans*, 109, C01009.

Large, W.G., McWilliams, J.C. and Doney, S.C. (1994) Oceanic vertical mixing: a review and a model with a nonlocal boundary layer parameterization. *Reviews of Geophysics*, 32, 363–403.

Lindsay, R.W. and Zhang, J. (2006) Assimilation of ice concentration in an ice–ocean model. *Journal of Atmospheric and Oceanic Technology*, 23, 742–749.

Losch, M., Menemenlis, D., Campin, J.-M., Heimbach, P. and Hill, C. (2010) On the formulation of sea-ice models. Part 1: effects of different solver implementations and parameterizations. *Ocean Modelling*, 33, 129–144.

Marshall, J., Adcroft, A., Hill, C., Perelman, L. and Heisey, C. (1997) A finite-volume, incompressible Navier stokes model for studies of the ocean on parallel computers. *Journal of Geophysical Research Atmospheres*, 102, 5753–5766.

Morison, J., Kwok, R., Peralta-Ferriz, C., Alkire, M., Rigor, I., Andersen, R. and Steele, M. (2012) Changing Arctic Ocean freshwater pathways. *Nature*, 481, 66–70.

Oke, P.R. and Sakov, P. (2008) Representation error of oceanic observations for data assimilation. *Journal of Atmospheric and Oceanic Technology*, 25, 1004–1017.

Proshutinsky, A., Krishfield, R., Timmermans, M.-L., Toole, J., Carmack, E., McLaughlin, F., Williams, W.J., Zimmermann, S., Itoh,

M. and Shimada, K. (2009) Beaufort gyre freshwater reservoir: state and variability from observations. *Journal of Geophysical Research Atmospheres*, 114, C00A10.

Proshutinsky, A., Krishfield, R., Toole, J.M., Timmermans, M.-L., Williams, W., Zimmermann, S., Yamamoto-Kawai, M., Armitage, T.W.K., Dukhovskoy, D., Golubeva, E., Manucharyan, G.E., Platov, G., Watanabe, E., Kikuchi, T., Nishino, S., Itoh, M., Kang, S.-H., Cho, K.-H., Tateyama, K. and Zhao, J. (2019) Analysis of the Beaufort gyre freshwater content in 2003–2018. *Journal of Geophysical Research Atmospheres*, 124, 9658–9689.

Ricker, R., Hendricks, S., Kaleschke, L., Tian-Kunze, X., King, J. and Haas, C. (2017) A weekly Arctic sea-ice thickness data record from merged CryoSat-2 and SMOS satellite data. *The Cryosphere*, 11, 1607–1623.

Rose, S.K., Andersen, O.B., Passaro, M., Ludwigsen, C.A. and Schwatke, C. (2019) Arctic Ocean sea level record from the complete radar altimetry era: 1991–2018. *Remote Sensing*, 11, 1672.

Sakov, P., Counillon, F., Bertino, L., Lisæter, K.A., Oke, P.R. and Korablev, A. (2012) TOPAZ4: an ocean-sea ice data assimilation system for the North Atlantic and Arctic. *Ocean Science*, 8, 633–656.

Schauer, U., Beszczynska-Möller, A., Walczowski, W., Fahrbach, E., Piechura, J. and Hansen, E. (2008) Variation of measured heat flow through the Fram Strait between 1997 and 2006. In: *Arctic–Subarctic Ocean Fluxes*. Dordrecht: Springer.

Semtner, A.J. (1976) A model for the thermodynamic growth of sea ice in numerical investigations of climate. *Journal of Physical Oceanography*, 6, 379–389.

Serra, N., Käse, R.H., Köhl, A., Stammer, D. and Quadfasel, D. (2010) On the low-frequency phase relation between the Denmark Strait and the Faroe-Bank Channel overflows. *Tellus A: Dynamic Meteorology and Oceanography*, 62, 530–550.

Skagseth, Ø., Furevik, T., Ingvaldsen, R., Loeng, H., Mork, K.A., Orvik, K.A. and Ozhigin, V. (2008) Volume and heat transports to the Arctic Ocean via the Norwegian and Barents Seas. In: *Arctic–Subarctic Ocean Fluxes*. Dordrecht: Springer.

Spreen, G., Kaleschke, L. and Heygster, G. (2008) Sea ice remote sensing using AMSR-E 89-GHz channels. *Journal of Geophysical Research: Oceans*, 113, C02S03.

Stammer, D., Balmaseda, M., Heimbach, P., Köhl, A. and Weaver, A. (2016) Ocean data assimilation in support of climate applications: status and perspectives. *Annual Review of Marine Science*, 8, 491–518.

Stammer, D., Köhl, A., Vlasenko, A., Matei, I., Lunkeit, F. and Schubert, S. (2018) A pilot climate sensitivity study using the CEN coupled adjoint model (CESAM). *Journal of Climate*, 31, 2031–2056.

Steele, M., Morley, R. and Ermold, W. (2001) PHC: a global ocean hydrography with a high-quality Arctic Ocean. *Journal of Climate*, 14, 2079–2087.

Uotila, P., Goosse, H., Haines, K., Chevallier, M., Barthélemy, A., Bricaud, C., Carton, J., Fučkar, N., Garric, G., Iovino, D., Kauker, F., Korhonen, M., Lien, V.S., Marnela, M., Massonnet, F., Mignac, D., Peterson, K.A., Sadikni, R., Shi, L., Tietsche, S., Toyoda, T., Xie, J. and Zhang, Z. (2019) An assessment of ten ocean reanalyses in the polar regions. *Climate Dynamics*, 52, 1613–1650.

Woodgate, R.A., Weingartner, T.J. and Lindsay, R. (2012) Observed increases in Bering Strait oceanic fluxes from the Pacific to the Arctic from 2001 to 2011 and their impacts on the Arctic Ocean water column. *Geophysical Research Letters*, 39, L24603.

Xie, J., Bertino, L., Counillon, F., Lisæter, K.A. and Sakov, P. (2017) Quality assessment of the TOPAZ4 reanalysis in the Arctic over the period 1991–2013. *Ocean Science*, 13, 123–144.

Xie, J., Counillon, F. and Bertino, L. (2018) Impact of assimilating a merged sea-ice thickness from CryoSat-2 and SMOS in the Arctic reanalysis. *The Cryosphere*, 12, 3671–3691.

Zhang, J. and Hibler, W. (1997) On an efficient numerical method for modeling sea ice dynamics. *Journal of Geophysical Research: Oceans*, 102, 8691–8702.

Zweng, M.M., Reagan, J.R., Seidov, D., Boyer, T.P., Locarnini, R.A., Garcia, H.E., Mishonov, A.V., Baranova, O.K., Weathers, K.W., Paver, C.R. and V, S. I. (2018) In: Levitus, S. and Mishonov, A. (Eds.) *World Ocean Atlas 2018, Volume 2: Salinity*, Vol. 82. Maryland: NOAA Atlas NESDIS, p. 1–50.

How to cite this article: Lyu G, Koehl A, Serra N, Stammer D, Xie J. Arctic ocean–sea ice reanalysis for the period 2007–2016 using the adjoint method. *Q J R Meteorol Soc*. 2021;147:1908–1929. https://doi.org/10.1002/qj.4002

APPENDIX A

Because of the nonlinear thermodynamic sea ice submodel, the adjoint sensitivities may suffer from strong sensitivities, which hamper the minimization algorithm. Figure A1a and c show such a case in which strong sensitivities of 2-m air temperature appear in the Kara Sea (black box region in Figure A1a) from June 20, 2007 to June 27, 2007 (black line in Figure A1c).

Here, we use a filter to suppress these large sensitivities. For one sensitivity variable, the filter compares the absolute value at a location with the global mean of its absolute value and with the mean absolute value of the surrounding eight grid points. We set the sensitivity to zero if the sensitivity is 30 times larger than the global mean of its absolute value or 10 times larger than the mean of the absolute values of the surrounding points. The filter algorithm is available at https://github.com/guokun-lyu-SJTU/MITgcm-sea-ice-DA/blob/main/filter_margin.F.

In the adjoint of the thermodynamic sea ice model, we apply the filter to the sensitivity variables of ice drift vectors, SST, SSS, net heat flux, effect snow thickness, SIC, and effective sea ice thickness to each timestep, thereby suppressing the strong local sensitivities, and the filter is also used to remove strong sensitivities of wind stress and net short wave radiation. The filter suppresses the regional strong sensitivities (Figure A1b and red line in Figure A1c) successfully and, at the same time, it has little impact on the adjoint sensitivities in the other regions.

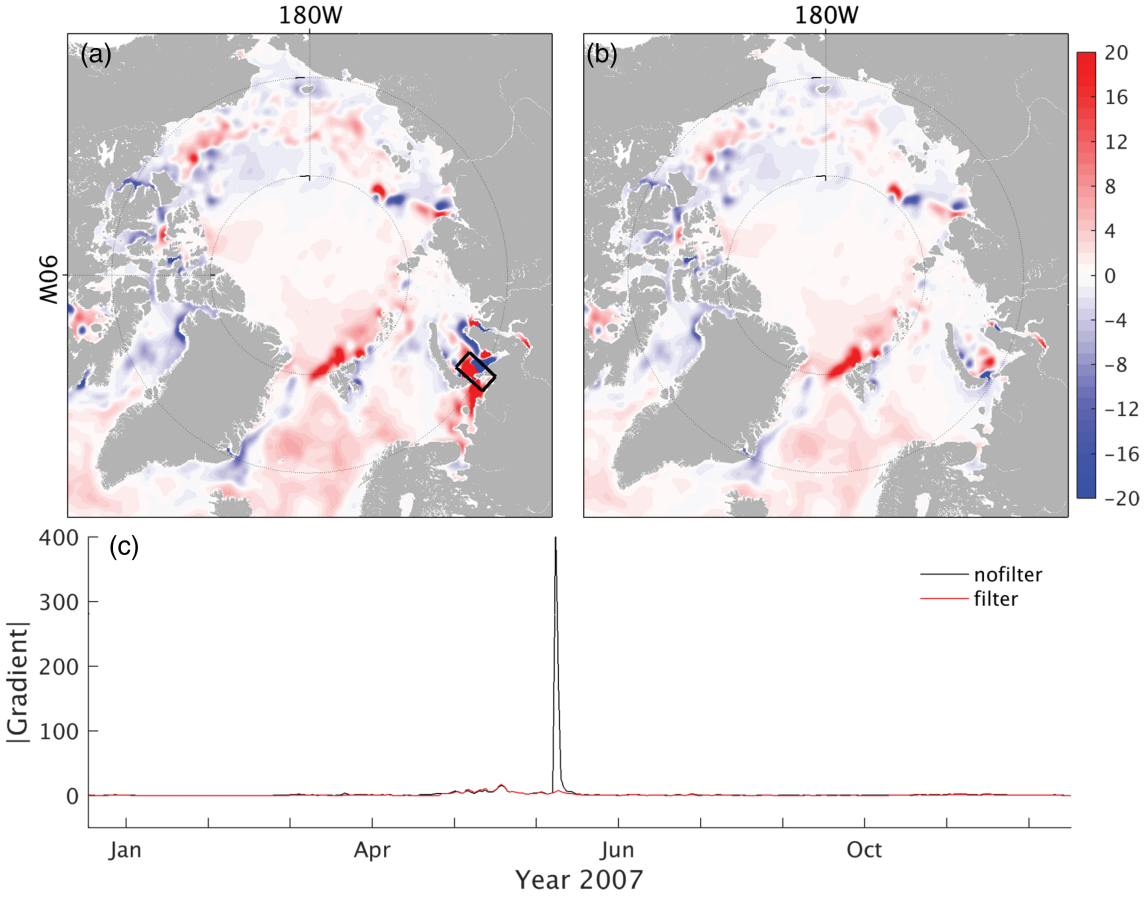

FIGURE A1 Adjoint sensitivity to 2-m air temperature on June 24 of the year 2007 (a) without and (b) with the filter. Panel (c) shows the mean absolute value of the sensitivity in the Kara Sea (enclosed by the black box in panel (a)) [Colour figure can be viewed at wileyonlinelibrary.com]